EUROFUSION WPHCD-PR(15) 13538

Simonin Alain et al.

R&D around a photoneutralizer based NBI system for the future fusion reactor

Preprint of Paper to be submitted for publication in
Nuclear Fusion

This work has been carried out within the framework of the EUROfusion Consortium and has received funding from the Euratom research and training programme 2014-2018 under grant agreement No 633053. The views and opinions expressed herein do not necessarily reflect those of the European Commission.

R&D around a photoneutralizer based NBI system for the future fusion reactor

A. Simonin[a], Jocelyn Achard[i], K. Achkasov[a, j], S. Bechu[h], C. Baudouin[a],O. Baulaigue[a], C. Blondel[e], JP. Boeuf[f], D. Bresteau[e], G. Cartry[j], W. Chaibi[b], C. Drag[e], H.P.L. de Esch[a], D. Fiorucci[a,b], G. Fubiani[f], I. Furno[c], R. Futtersack[f,] P. Garibaldi[a], A. Gicquel[i], C. Grand[a], Ph. Guittienne[l], G. Hagelaar[f], A. Howling[c], R. Jacquier[c], M.J. Kirkpatrick[k], D. Lemoine[d], B. Lepetit[d], T. Minea[g], E. Odic[k], A. Revel[g], B.A. Soliman[m], P. Teste[k].

[a] *CEA, IRFM, F-13108 St Paul lez Durance, France.*
[b] *Laboratoire ARTEMIS-UMR CNRS 7250, Cote d'Azur Observatory, Nice, France.*
[c] *Ecole Polytechnique Fédérale de Lausanne, Centre de Recherches en Physique des Plasmas CH-1015 Lausanne, Switzerland*
[d] *Université de Toulouse, Université Paul Sabatier, Laboratoire Collisions Agrégats Réactivité, IRSAMC(LCAR); CNRS, UMR 5589, F-31062 Toulouse, France*
[e] *Laboratoire Aimé-Cotton (LAC), CNRS, université Paris-Sud, école normale supérieure de Cachan, bât. 505, F-91405 Orsay cedex.*
[f] *Laboratoire Plasma et Conversion d'Energie, LAPLACE, P. Sabatier University, F- Toulouse, France.*
[g] *Laboratoire de Physique des Gaz et des Plasmas, LPGP,UMR 8578 : CNRS- Paris-Sud University, F-91405 Orsay, France.*
[h] *LPSC, Université Grenoble-Alpes, CNRS/IN2P3, F-38026 Grenoble France*
[i] *Laboratoire des Sciences des Procédés et des Matériaux; LSPM, CNRS-UPR 3407 Université Paris 13, F-93430 Villetaneuse ; Labex, SEAM, PRES Sorbonne Paris Cité, France*
[j] *Laboratoires de Physique des Interactions Ioniques et Moléculaires ; PIIM ; Aix-Marseille University, CNRS, UMR 7345, 13013 Marseille, France*
[k] *Laboratoire Génie Electrique, Electronique de Paris, GeePs, CNRS UMR 8507, CentraleSupélec, UPSud Université Paris-Saclay and UPMC Sorbonne Université, 91192 Gif-Sur-Yvette, France*
[l] *Helyssen Sàrl, Route de la Louche 31, CH-1092 Belmont, Switzerland.*
[m] *Accelerators and Ion sources Department, Nuclear Research Center (NRC), Atomic energy Authority. P.O. Box: 13759 Inchas, Atomic Energy, Cairo, Egypt.*

Abstract. Since the signature of the ITER treaty in 2006, a new research programme targeting the emergence of a new generation of NBI system for the future fusion reactor (DEMO) has been underway between several laboratories in Europe. The specifications required to operate a NBI system on a Fusion reactor (DEMO) are very demanding: the system has to provide plasma heating, current drive and plasma control at a very high level of power (up to 150 MW) and energy (1 or 2 MeV), including high performances in term of wall-plug efficiency ($\eta > 60\%$), high availability and reliability. To this aim, a novel NBI concept based on the photo-detachment of the energetic negative ion beam is under study. The keystone of this new concept is the achievement of a photo-neutralizer where a high power photon flux (~3 MW) generated within a Fabry Perot cavity will overlap, cross and partially photo-detach the intense negative ion beam accelerated at high energy (1 or 2 MeV). The aspect ratio of the beam-line (source, accelerator, etc…) is specifically designed to maximize the overlap of the photon beam with the ion beam. It is shown that this new concept has the capability to provide several tens of MW of D^0 per beam line with a wall-plug efficiency higher than 60% leading to a significant reduction of the cost (a factor 2) of the NBI system. A feasibility study of the concept has been launched between different laboratories to address the different physics aspects, i.e., negative ion source, plasma modelling, ion accelerator simulation, photoneutralization and high voltage holding under vacuum. The paper describes the present status of the project and the main achievements of the developments in laboratories.

Keywords: Ion source, plasma modelling, Photo-detachment, Fabry-Perot cavity, Electrostatic accelerators, negative ions, neutral beams, high voltage holding in vacuum, DEMO.

INTRODUCTION

The construction of ITER raises the question of the next step toward a real fusion power plant, DEMO, which should be the first fusion reactor to demonstrate electricity production over long periods. In order to produce the required 500 MW of electricity coupled to the grid [1,2], the fusion reactions have to provide 1.5 GW of thermal power. Additional heating systems must be implemented in the reactor system in order to provide the initial plasma heating to enter the burn phase; the heating power required for a pulsed machine with no (or low) current drive is 50 MW while for a quasi-steady state reactor (pulse length of 300h) with a high current drive level [3,4,5] no less than 150 MW is required. Two heating systems are being so far considered for DEMO: the neutral beam injection (NBI) system which injects high-energy neutral atoms into the plasma core, and the electron cyclotron resonance heating (ECRH) system which accelerates electrons in the plasma core via electromagnetic waves (f~170 GHz). The overall power efficiency of these plasma heating systems becomes an important parameter for a power plant as it directly impacts on the net electrical power produced by the reactor and the electricity cost. While with the present device (the ITER NBI system), the efficiency is lower than 30% [6], a tolerable electricity cost produced by a fusion reactor (DEMO) requires a global wall-plug efficiency higher than 60% [7].

It is clear that the NBI system remains an essential part of a reactor device, with very stringent requirements, such as the realisation of powerful high-energy beams, i.e., several tens of MW of neutral power at an energy ranging between 1 (for the pulsed machine) and 2 MeV (for the long pulse reactor), high wall-plug efficiency (> 60%) and a small footprint on the reactor environment. The achievement of such a performance requires considerable R&D effort in parallel to the ITER construction.

Presently, the NBI systems' negative ion beam neutralization is achieved by the stripping of the extra electron from negative ions through collisions with gas injected into the neutralizer cell. It is a simple and reliable method, but the neutralization efficiency is modest (around 55%) and the amount of gas injected both in the source and neutralizer leads to a high background gas density within the accelerating channel such that in the ITER-NBI system, about 30% of the negative ions being accelerated are lost [8] due to molecular collisions thus contributing to the poor injector efficiency.

The neutralization of high-energy negative ions by photo-detachment (photoneutralization) is an attractive alternative to beam neutralization by a gas target for several reasons [9,10]: a potentially high beam neutralization rate (higher than 80%), a complete suppression of the gas injection in the neutraliser, which amounts to 80% of the total gas injected along the ITER-beamline [6], reduction of stripping losses in the accelerator and reduction in parasitic particles (electrons, neutrals, positive ions) generated inside and outside the accelerator which load the beamline components.

On the other hand, it is a challenging method which requires significant R&D efforts before considering its implementation on an NBI system; indeed, due to the low photodetachment cross-section (about $4.3\ 10^{-21}$ m^2) and a weak interaction time [9,10,11], a high photon flux (higher than 10MW of laser power) is required to attain a high neutralization rate (>80%).

Previous studies on photoneutralization [12] have shown that light flux amplification can be achieved in an optical Fabry-Perot cavity set across the ion beam, to a factor high enough to achieve around 3MW of photon power, within realistic experimental parameters. The orders of magnitude would be a cavity finesse of 10000 fed by an amplified single-mode CW ~1 kW range laser. The duplication of such cavities (3 to 5 cavities) along the D^- beam within the photoneutralizer cell would result in the required high neutralization.

This new injector concept is a break from the conventional devices based on gas neutralization; it leads to the emergence of dedicated R&D in different fields of physics in order to cover all the different injector aspects: ion source& accelerator (this paper), photo-detachment physics [9,10,11], high power Fabry-Perot cavity [11,12], caesium-free negative ion formation [13,14], and R&D on high voltage holding under vacuum [15,16].

After a presentation of the injector concept (chapter 1), this paper highlights the accompanying R&D in the different laboratories in France: chapter 2 describes the developments around a dedicated negative ion source which fits with the Siphore geometry (experiences and modelling); chapter 3 addresses 2D & 3D simulations of the ion beam in the accelerator, photoneutralizer and energy recovery system; chapter 4 presents the R&D and advances in photoneutralization (photo-detachment physics and the development of a high power Fabry-Perot cavity), and chapter 5 describes an ongoing project targeting the development of a new high voltage bushing for Siphore with accompanying studies in high voltages holding under vacuum.

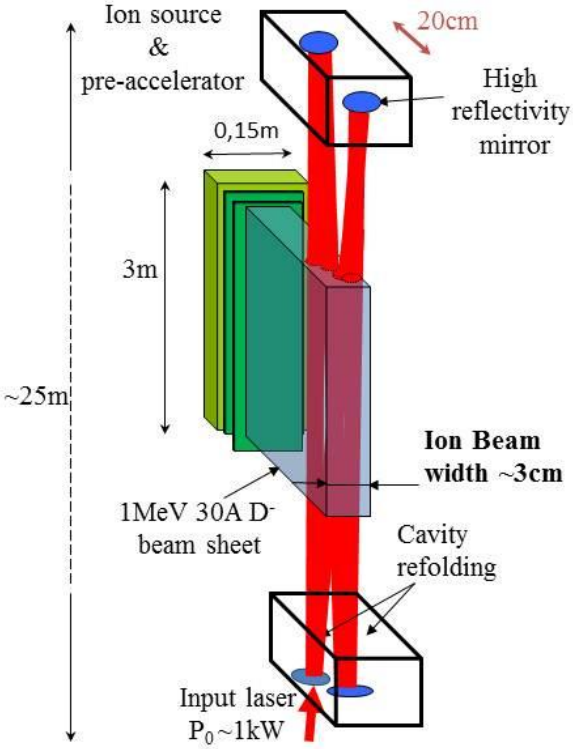

Figure 1.1: Topology of a photoneutralization based injector

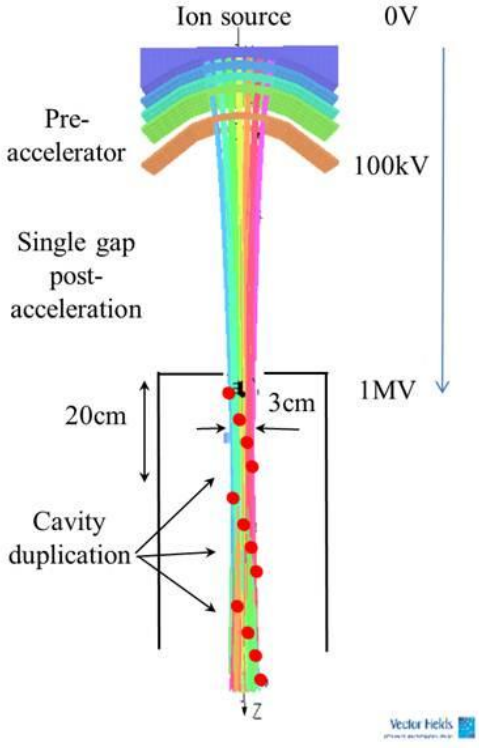

Figure 1.2: 3D simulation of the D^- beam optics: pre-acceleration at 100 keV of seven beamlets in curved grids and post acceleration in a single gap at 1MeV.

1-SIPHORE CONCEPT

The interaction of the photon beam with the high energy ion beam has to be maximized by a specific design and aspect ratio of the beam line (see Fig. 1.1); the source & accelerator have to provide a thin and intense ion beam sheet (~30 A of D^- at 1 or 2 MeV) in the neutralization region which has to be entirely overlapped and crossed from side to side by the photon beam [11,12]. As a direct consequence, this negative ion beam sheet is provided by an ion source and accelerator whose dimensions (~3 m high, ~15 cm wide) and concepts significantly differ from conventional NBI systems (ITER). Figure 1.2 shows a 3D simulation (top view) of the accelerator, the negative ions are pre-accelerated up to 100keV, and merged into a single macro beam in the post-acceleration gap, in order to form a thin ribbon beam. The photoneutralizer is an equipotential cell held at 1MV, the stripped electrons at an energy of 270eV (1MeV/3672) released by the photo-detachment are trapped by the 1MV potential well and dumped, the secondary plasma density formed by the interaction of the charged particles (D^- beam & electrons) with the background gas (~5mPa) is low (n_e~10^{16} m^{-3}) leading to a positive ion (D^+) current leakage from the apertures in the mA range (I_{D^+}<10mA).

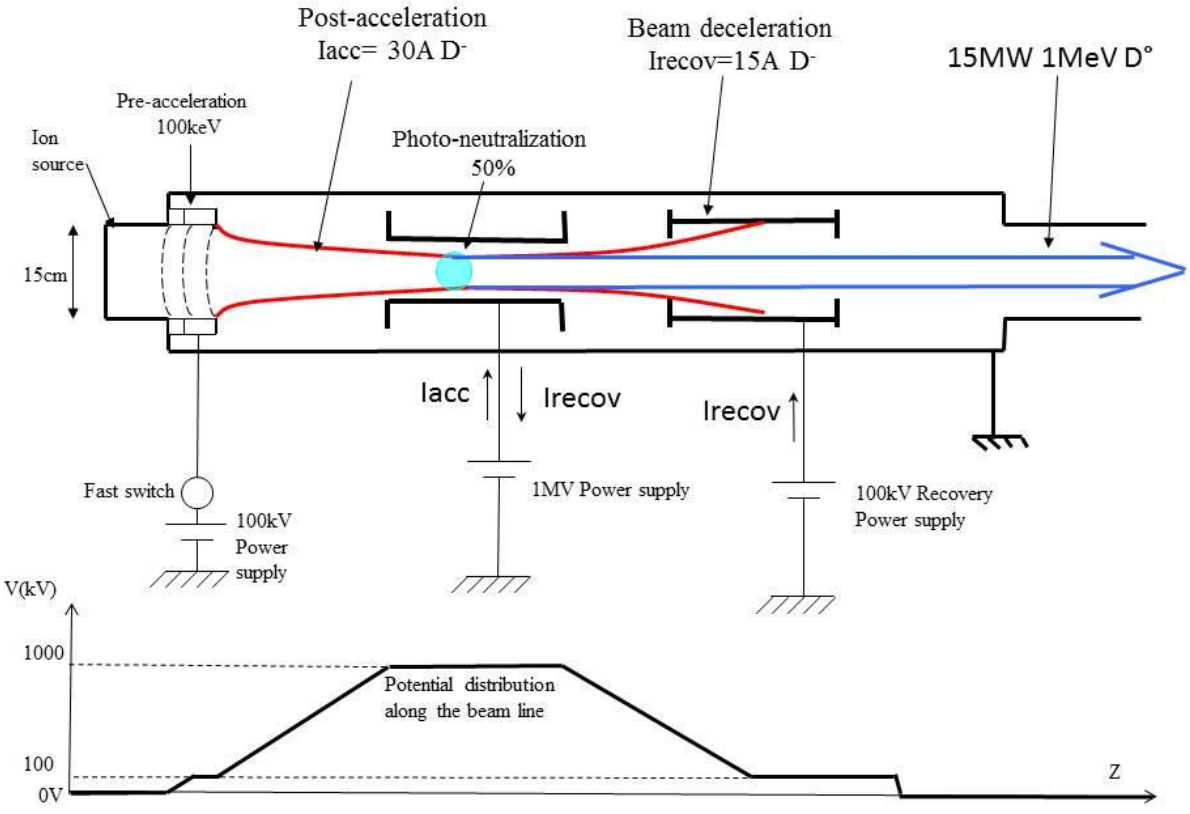

Figure 1.3: Principle of a 1MeV Siphore injector (Top view), and potential distribution along the beam line. The source is grounded and the photoneutralizer is held at +1MeV.

At the photoneutralizer exit, the 1 MeV non-neutralized fraction of negative ions (D^-) are decelerated down to a low energy (<100 keV) and collected on the recovery electrode; the electrostatic force being conservative, the load (current) of the high voltage (1MV) power supply is then reduced. In this way high injector efficiency is reached even with incomplete photo-neutralization. In summary, the injector concept is composed of a SIngle gap 1MeV accelerator, followed by a PHOtoneutralizer and a Recovery Energy system, leading to the acronym SIPHORE.

Figure 1.1 also shows that a complete illumination (overlap) of the D^- beam can be achieved by a cavity refolding (~3 to 4 refoldings) which steers the photon beam transversally. We note that it is a compact system in the direction parallel to the ion beam (see figure 1.1) with a width of 20cm. The photodetachment area is located at the ion beam waist (figure 1.2) close to the photoneutralizer entrance where the divergence is minimal (θ<10mrad). Moreover, as the space charge force decreases with increasing beam energy (1 or 2MeV), several adjacent, identical and independent cavities along the beam waist region can be implemented increasing the effective laser power (and the overall neutralization rate), i.e., three adjacent cavities of 3MW each providing a neutralization rate of 50% leading to a total neutralization rate of 87.5% at 1MeV.

1MeV injector efficiency evaluation: For this assessment, we assume:

-i) A D^- beam (I_{D^-}=30A) accelerated at 1MeV with N=87.5% of photodetachment provided by three adjacent Fabry-Perot cavities, and a recovery electrode which collects the non-neutralized fraction $I_{recov}=I_{D^-}*(1-N)$= 3.75A of D^- at E_{recov}=100 keV => P_{recov}=0.37 MW

-ii) P_{duct}=20% transmission losses of the 1MeV neutrals in the duct (including beam re-ionization)

-iii) Other electrical power losses: P_s=1MW to supply the source and pre-accelerator, P_{sub}=2MW for the subsystems (pumping and cooling systems), and η_{ps}=90% efficiency of the 1M power supply

-iv) The CW single mode laser power feeding the optical cavity being in the range of a few kW is negligible.

The wall plug efficiency η_{wp} is the ratio of the neutral power injected in the plasma by the total electrical power consumed to produce this neutral beam:

Eq.1: $$\eta_{wp} = \frac{I_{D-} * N * (1-P_{duct})}{\frac{I_{D-} * N}{\eta_{ps}} + P_{recov} + P_{sub} + P_s} = 0.64$$

The system would provide 21MW of neutral beam at 1MeV injected in the plasma core, for an overall injector efficiency close to 64%.

1.2) Towards a 2 MeV high efficiency NBI system :

Neutral beams at 2MeV have significant advantages with respect to 1MeV beams; indeed, the increase by a factor two of the neutral power with the same extracted D^- current (reduction of the number of beamlines), and an increase of 40% of the non-inductive current drive [17] by respect to a 1MeV beam.

The Siphore concept allows an increase in beam energy up to 2MeV via a tandem configuration (see figure 1.5) where the ion source and pre-accelerator are held at -1MV, separated from the neutralizer at +1MV by a central grounded electrode. The 1MV electrical set

up (1MV power supplies, bushing, etc.) is symmetrical with opposite polarities on both sides of the grounded electrode. The source and pre-accelerator are suspended under vacuum and powered through the -1MV bushing; they provide the ion beam sheet which is then post-accelerated in two steps towards the photo-neutralizer at +1MV. The unneutralized negative ions (at 2 MeV) will be deflected out from the neutral beam, decelerated up to 100keV and collected on a cooled target polarized at -900kV.

Moreover, since the photodetached fraction is a function of the time of flight of the negative ion in the photon beam, it decreases by a factor $\sqrt{2}$ at 2MeV leading to only 35% of neutralization ratio (instead of 50% at 1MeV) with a 3MW photon beam. The duplication of several cavities along the ion beam will compensate for this decrease (5 cavities ⇔ 88% of theoretical neutralization rate).

We note on figure 1.5 that the optical components (cavity mirrors) are located far away from the injector (~15m away) and outside the nuclear island of the beam line and Tokamak in order to prevent them from any pollutants (plasma-gas-metallic sputtering, radiation). Intermediate active pumping cells and absorbing materials would contribute to keep the optical cells under high and clean vacuum conditions ($P_{optical\ cell}$~10^{-6}Pa).

2MeV injector efficiency : Again, we assume:

-i) A 30A D^- beam accelerated at 1MeV with 88% of photodetachment provided by five adjacent Fabry-Perot cavities, and a recovery electrode which collects the non-neutralized fraction (4A) of D^- at 100keV (~400kW of thermal load) on the -900kV recovery electrode (see Fig. 1.5 and paragraph 3-3).

-ii) 20% transmission losses of the 2MeV neutrals in the duct (including beam re-ionization); we note that re-ionization cross section at 2MeV are lower than at 1MeV; indeed, the cross section for the formation of positive ions in collision of the energetic D°(f) with gas (D_2),

$D°(f) + D_2 \rightarrow D^+(f) + D_2 + e^-$, is maximum at 20keV and monotony decreases at higher energy. At 1MeV, the cross section is $\Gamma(1MeV)=3.68E^{-17}cm^2$, and at 2MeV, $\Gamma(2MeV)=1.91E^{-17}cm^2$.

-iii) Other electrical power losses: 1MW to supply the source and pre-accelerator, 2MW for pumping and cooling systems, and 90% efficiency of the 1MV power supply

The system would provide 42MW of neutral beam at 2MeV injected in the plasma core, for an overall injector efficiency close to 68%.

1-2) Cost reduction with a high efficiency photoneutralized based NBI system:

The efficiency is the main factor impacting of the cost:

-a) The direct cost of the NBI system, i.e., $ per Watt of neutral power, is mainly due to the 1MV power supply and its electrical set up which amounts to about 70% of the overall cost of the beamline; indeed, a 60MW 1MV power supply which provides 17MW of 1MeV D° beam on ITER could supply two 30A "Siphore beamlines" implemented in parallel within the same vacuum tank to provide 42MW (2x 21MW) of D° at 1MeV

-b) For a quasi-steady state reactor with a high current drive level [3,4,5], the required heating power ranges around 150MW; at this level, the recirculating electrical power within the plant (to supply the heating systems) becomes significant and impacts on the electricity cost [7]; as a direct consequence, the wall-plug efficiency will have to be the highest as possible ($\eta >>$ 60%).

The ways which lead to a high wall-plug efficiency (see Eq. 1) are:

-i) A neutralization rate N much higher than 80%

-ii) An efficient energy recovery system to collect the residual (non-neutralized) negative ions at a low energy

-iii) A drastic reduction of the neutral beam transmission losses within the duct (P_{duct}) by minimizing the neutral beam divergence (< 5mrad), the optic aberrations and the neutral re-ionization by the background gas in the duct.

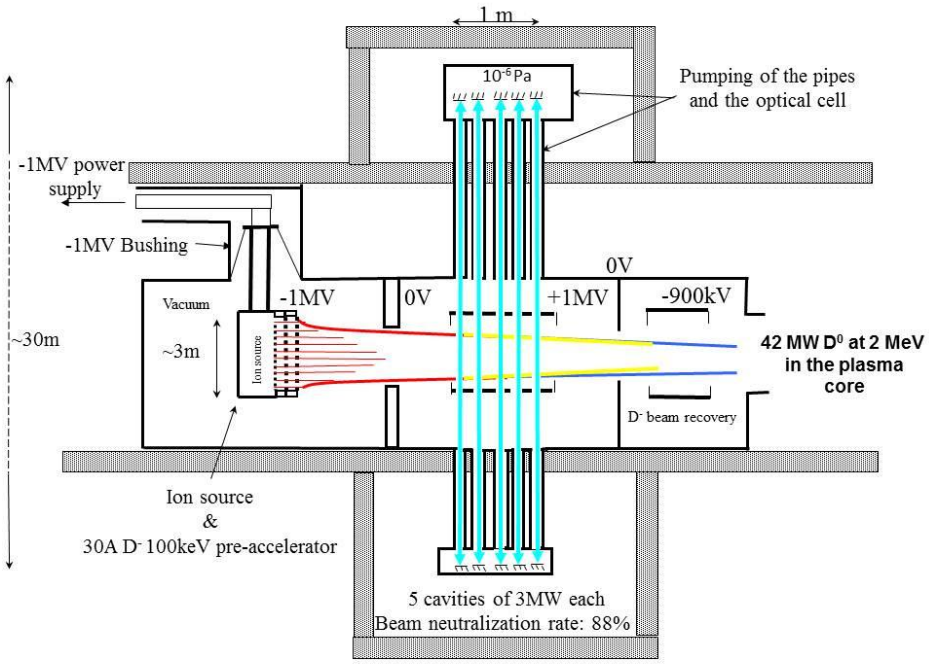

Figure 1.5: Side view of a 2MeV Siphore injector, with the source at -1MV and the photoneutralizer at +1MV; the ion source and pre-accelerator are sustained under vacuum polarized at -1MV and supplied by a vertical bushing. The photoneutralizer and recovery cells are sustained under vacuum by lateral Bushings (not shown on the figure) at +1MV and -900kV respectively.

2- ION SOURCE DEVELOPMENT FOR SIPHORE

Conventional negative ion sources [18] used for NBI systems are based on either filaments or on radio frequency (RF) heating. All make use of caesium to produce sufficient amounts of negative ions. Conventional RF sources are ICP (Inductively Coupled Plasma) driven ion sources where several RF plasma generators (called Drivers) at the back of the source produce a hydrogen or deuterium plasma which bombards through a transverse magnetic field (called filter field) the first accelerator electrode, called the Plasma Grid (PG), where negative ions are formed and extracted. The filter field acts as a magnetic barrier which cools down the hot electrons generated within the drivers and prevents a high rate of destruction of the negative ions formed on the PG. The source has to produce high and uniform current density (J_{D^-} = 250 $A.m^{-2}$ with ±10% of homogeneity) over a large extraction area (~ 0.8 m^2 on ITER) at a low operating

pressure (p < 0.3 Pa) to limit the negative ion losses by stripping reactions in the accelerator. Past experiments of source prototypes [19] and plasma modelling [20-24] have shown that a plasma drift occurs along the vertical axis due to diamagnetic effects leading to significant plasma inhomogeneity (along the vertical axis) in the extraction region. As a direct consequence, this source concept with the transverse filter field which leads to a significant plasma inhomogeneity along the vertical axis is not suitable for a long (~2.5m height) and thin (~15cm wide) Siphore ion source.

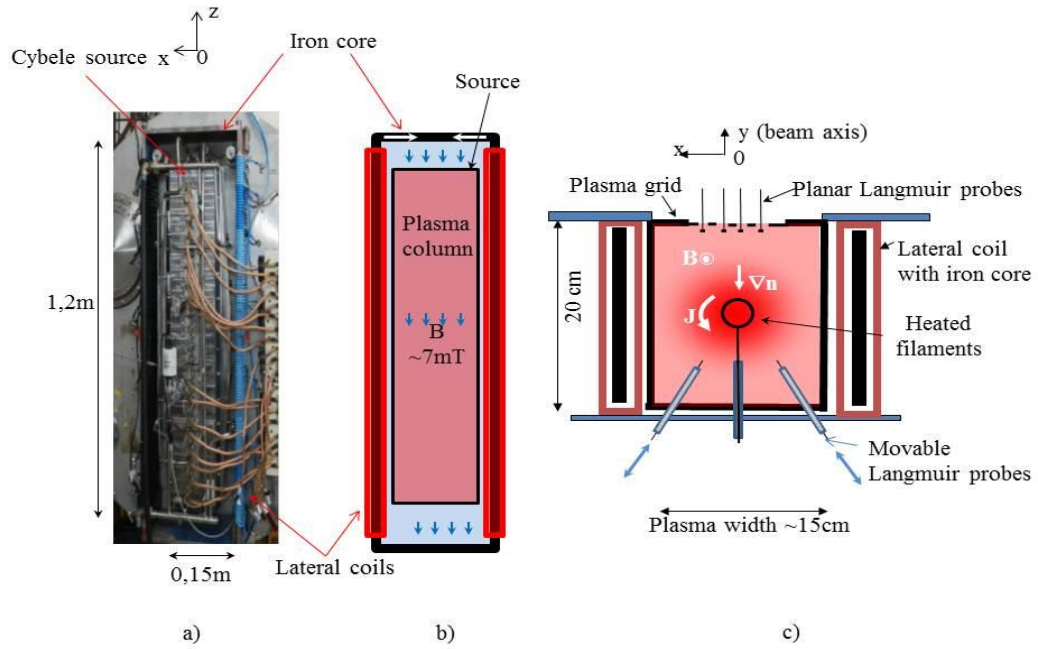

Figure 2.1: a) Photo of the Cybele source with the surrounding iron core and lateral magnets; b) Schematic of the magnetic field (arrows); c) Horizontal cross section of the source

A new source concept is under investigation at IRFM. The Cybele ion source [25] is a tall and narrow ion source (see figure 2.1-a) with a rectangular aspect ratio that is particularly relevant to Siphore; its plasma source dimensions are: height 1.2m, width 15cm, depth 20cm. Cybele is a filamented plasma source in which 5 sets of 3 tungsten filaments are used as cathodes (Vcathode=-70V) along the source vertical axis. The filaments supply the plasma core with primary electrons along the vertical axis (see figure 2.1-c); the filament current ranges from 200 to 1500A (power up to 100kW); the source walls are connected to the ground potential. A uniform magnetic field parallel to the source vertical axis is generated by two lateral electric coils sitting on opposite sides of an iron rectangular frame which surrounds the source (see figures 2.1-b). The two coils generate magnetic fields in the opposite direction inside the iron structure (see figure 2.1-b). It is the leakage field between the two coils that then fills uniformly the plasma source volume. The magnetic field intensity can be adjusted between 0 and 7 mT by adjusting the DC electric current in the coils.

In the plasma column, charged particles are not magnetized identically. For a magnetic field intensity of 7 mT, the Larmor radius of 70 eV primary electrons is only 4 mm whereas 0.5 eV D^+ ions gyrate within a 21 mm radius. These particles gyrate around the magnetic field lines and diffuse according to their respective mobility. Electrons moving freely around magnetic field

(B) lines will leak at the source extremities (top and bottom) due to the open magnetic field lines, and make the plasma density along the column uniform. Perpendicularly to the magnetic field lines the electron transport is impeded and occurs mainly due to collisions. In this geometry density gradients obviously exist, between the center of the source where heated filaments are located and the source walls where ions recombine. These density gradients produce potential gradients. Ions move slower than electrons along the magnetic field due to their lower thermal velocity, but their radial diffusion is faster. The fact that ions diffuse preferentially radially while electrons escape along the field lines is a rather interesting behavior for a negative ion source which must extract a high negative ion current with a low co-extracted electron rate (less than 1e- per D^-). The first phase of experiments on Cybele were carried out with a heated filament polarized at -70 V at pressures ranging from 0.12 Pa to 0.26 Pa in pure hydrogen.

An array of 30 planar Langmuir probes, attached to the plasma grid at the source front (see figure 2.1-c), allows for the measurement of the vertical and transverse plasma density distribution in the extraction area. Two cylindrical probes can move horizontally, they are installed at the back plate of the source and allow measurements of the radial distribution of plasma parameters from the edge (source wall) up to the plasma centre. These parameters are the plasma (V_p) and floating potential (V_f), the electron density (n_e), the electron temperature (T_e) and the electron energy probability function (EEPF). In order to avoid plasma and sheath perturbations as predicted by probe theory [26], the probe size (0.8 mm in diameter and 10 mm in length) is smaller than both the electron mean free path (~10 cm) and the particle Larmor radius: at 5.3 mT, the Larmor radius of colder electrons (4 eV) is 1.3 mm. Moreover, the relative negative-ion density (n_i/n_e) in the plasma is negligible throughout the experimental period, and there is no Caesium injection into the plasma. Figure 2.2 a and b presents respectively the I(V) curve and the EEPF obtained at 9 cm from the source wall. The two-component electron population (hot and cold electrons) is clearly visible in the calculated EEPF (see Fig 2.2-b). Even though the cold component is close to a Maxwellian distribution (the circular dots presented on Fig. 2.2-b corresponding to the cold component of the EEPF is linear-like between 5 and 15 eV), the hot component (represented by star dots) of the EEPF (above 15 eV) is clearly non-Maxwellian (the hot component of the EEPF has no linear part).

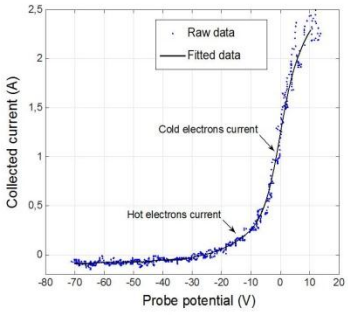

a)

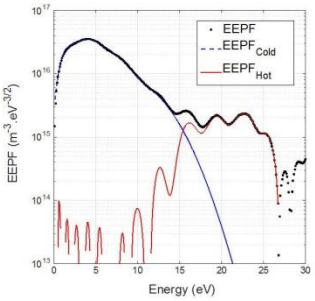

b)

Figure 2.2: a) Raw and fitted I(V) curves (square dots and continuous line respectively) obtained at 9 cm from the source wall for 6.5 mT. b) EEPF obtained from the fitted I(V) curve is presented.

2.1 Experimental results from the Cybele source (IRFM, LPSC Laboratory):

Figure 2.3 left shows radial profiles of plasma density (n_e) and effective electron temperature (T_e) for a power input of 30 kW with different magnetic field intensities. The Langmuir probe scans the plasma 3 cm from the source wall to 10 cm inside the source (the plasma centre) where primary electrons of 70 eV are emitted. We observe that the plasma density peaks in the source centre at field intensity at or above 3.7 mT; this effect is due to the increase of the electron confinement by the magnetic field (the Larmor radius of the 70eV electron is 5mm), such that the plasma density increases from 0.7×10^{17} m^{-3} up to 4.8×10^{17} m^{-3}. Figure 2.4 shows the electron temperature, we note a better plasma cooling with increasing field intensity.

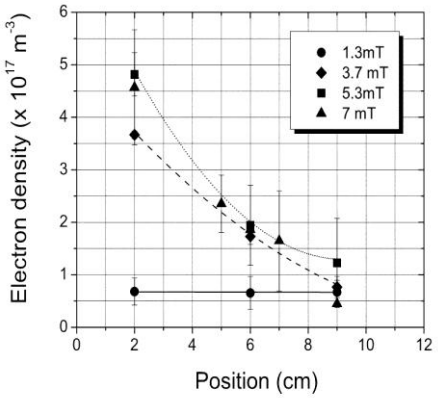

Figure 2.3: Radial profiles of electron density (ne) and effective electron temperature (Te) at different magnetic field intensities (1.3, 3.7, 5.3 and 7 mT). The source center is at 10 cm.

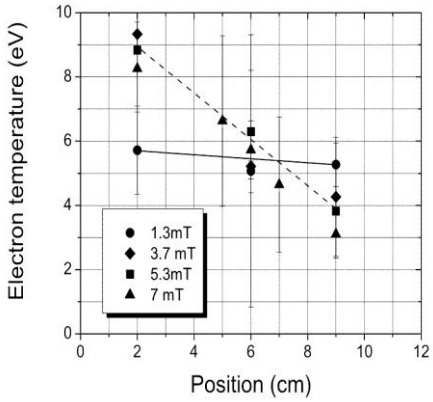

Figure 2.4 presents the variations of floating and plasma potentials from the source wall up to the centre at 6.5 mT and 3 mT ($P_{filaments}$ = 30 kW and source pressure 0.26 Pa).

The floating potential (V_f) is -48 V in the plasma centre close to the filament (see Fig. 2.5), suggesting the presence of hot electrons. Close to the source wall V_f is weaker (-14 V for B=3 mT). We also note in Figure 2.5 a negative plasma potential for the two magnetic field intensities of 3 and 6.5 mT which results from the fact the electron radial mobility is lower than that of the ions. With the decrease of the radial electron current diffusing across the B-field line scaling as ~1/B (Bohm diffusion [27]), the plasma potential becomes more negative to maintain the electron transport towards the source wall. At low magnetic fields, the plasma potential is nearly uniform (-10 V at 3 mT) in the plasma bulk, while at higher field intensity (6.5 mT), a radial electric field appears likely due to a diagmagnetic effect; this radial electric field could lead to rotating instabilities with an E × B drift [31].

The vertical and transverse plasma density distributions measured with the planar probes on the plasma grid are shown in figures 2.6 and 2.7 for B = 7mT, Pfilaments = 30kW and P=0.26 Pa. Along the source vertical axis (figure 2.6) the plasma density is nearly uniform but rapidly decreases over the last 10 cm at the source extremities due to the electron leak in the direction parallel to the B-field lines (due to the high electron mobility in the direction parallel to B).

Figure 2.5: Radial plasma potential distribution for two magnetic fields (3 and 6.5mT) from the source centre (position 1cm) up to the edge (12cm).

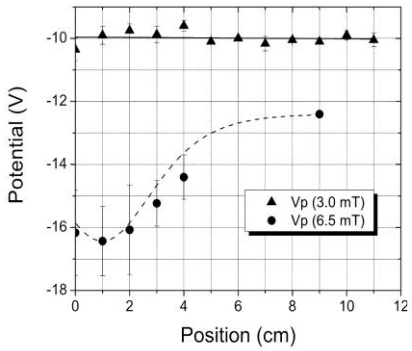

Figure 2.7 highlights an asymmetry in the transverse (right-left) plasma parameters: on the left side, the plasma has a higher density (by a factor of 2), higher electron temperature and floating potential than on the opposite side (right), as if the probes on the left side penetrate deeper in the plasma. An inversion of the magnetic field in the source induces the same asymmetry on the opposite direction.

The optimum source pressure is around 0.25Pa; at a lower pressure, the plasma density decreases while it saturates above (0.25Pa). A scan of the power intake up to 100 kW at 0.2 Pa (with B = 7 mT) shows a linear increase in plasma density from 2 1017m-3 up to 8 1017m-3; above this, the plasma density saturates.

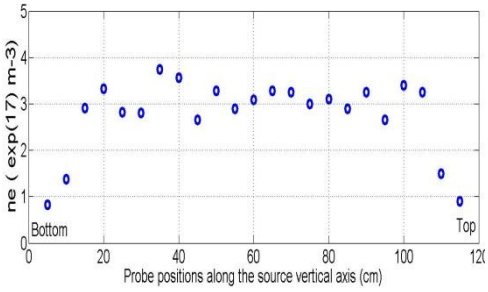

Figure 2.6: Plasma density along the vertical axis

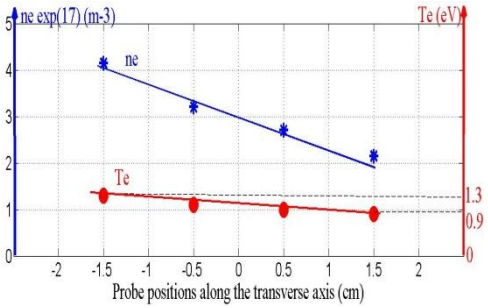

Figure 2.7: Transverse plasma profiles

2.2) 2D modeling of the Cybele source (LAPLACE laboratory)

Simulation of the Cybele source operation with filaments has been performed with the PIC MCC (Particle-In-Cell Monte Carlo Collisions) model described in Refs. [28-32]. The PIC MCC model is two-dimensional in the plane perpendicular to the magnetic field. As in Refs.[28-32], a discharge in pure H_2 is considered and no plasma chemistry is included in the model. A complete set of electron-H_2 collision cross-sections, charged exchange collisions of positive ions, and electron-ion Coulomb collisions are taken into account. Since it is practically impossible, with PIC simulations, to simulate steady state situations with plasma densities as large as 10^{18} m^{-3}, which are expected in Cybele, we consider smaller plasma densities (on the order of 10^{15} m^{-3}) and use a scaling factor. The Debye length (and sheath lengths) in the simulation are therefore

much larger than in the real plasma and care must be taken in the interpretation of the simulation results (especially in the presence of non-classical collisional plasma transport or plasma turbulence).

To account for the charged particle losses at the end walls, we proceed as follows. We assume that the electric potential along the magnetic field (in the direction parallel to the magnetic field) is constant (zero axial electric field). The electron trajectories are followed in the three directions (the electric field is calculated only in 2D, i.e. in the plane perpendicular to the magnetic field). When an electron reaches one of the end plates the electron is lost if its energy in the direction parallel to the magnetic field is larger than the potential drop between the plasma and the end plate (sheath voltage), otherwise it is reflected back in the plasma.

The ion losses are estimated by defining a loss frequency equal to $2u_B/L$ where $u_B=(kT_e/M)^{1/2}$ is the Bohm velocity deduced from the local electron temperature T_e. At each time step, a Monte Carlo technique is used to choose, according to this frequency, the ions that will be lost to the end walls assuming that the ions are distributed uniformly along the plasma column. The approximation of a uniform density along the plasma column could certainly be improved which would lead to a correcting factor in the ion loss frequency $2u_B/L$. We consider that this approximation is sufficient for the purpose of this work. The simulations have been performed in a cylindrical geometry, with a chamber diameter of 14 cm and a column length L of 1 m.

We first performed simulations where the filament cathodes were represented by a punctual source of electrons in the centre of the simulation domain. The sheath around the filament was not described and the electrons were supposed to be emitted with an energy equal to the potential difference between the plasma potential and the voltage applied to the filament (-70 V). This approach neglects the positive ion losses to the filaments (ions must be lost to the walls and end plates). The probe measurements performed in Cybele however show that the potential in the column is below the wall potential (see Fig. 2.5) and this suggests that the positive ions are not lost to the walls but to the filaments. We therefore modified the model description with electron emission by the filaments.

In the results presented below the filaments are represented by an electron emitting cylinder of diameter 1 cm. Positive ions can be collected by this cylinder. Since the real cathode sheath cannot be described accurately in the simulation (because the simulated plasma density is much lower than the real plasma density) electrons are supposed to be emitted at the cathode surface with an energy $E_b=eU_b$ close to (but lower than) the filament voltage while the potential of the filament is fixed at a negative value $-U_f$ with respect to the walls of the plasma column. (U_b+U_f) is fixed to 70 V in the simulation (with U_b=50Vand U_f=20V).

We consider this equivalent to a total potential drop of 70 V in the sheath, without describing the details of the sheath (and assuming that the surface of the cathode in the simulation actually represents the limit of the pre-sheath, with a potential fixed at 20 V).

Figures 2.8 shows the radial distribution of the normalized, time averaged plasma density for two values of the magnetic field, 3 mT and 5 mT calculated for a hydrogen pressure of 0.27

Pa. The densities are represented by a dotted line around the filament because of the approximate representation of the filament and sheath around the filament in the model. The unit for the plasma density in Fig. 2.8 is $2x10^{18}$ m^{-3} for 5 mT and slightly below for 3 mT. These values are obtained for a total (scaled) current of around 500 A, corresponding to a power of 35 kW (500 A x 70 V).

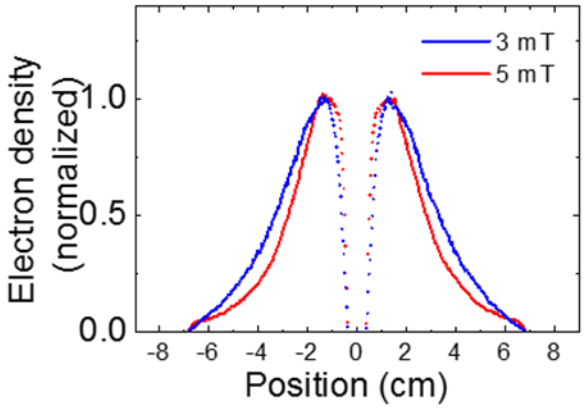

Figure 2.8: Radial distribution of the time averaged, normalized plasma density for two values of the magnetic field (3 and 5 mT) and a pressure of 0.26Pa.

In this power range, the experiments (see Fig. 2.3) give a much lower plasma density, on the order of $2x10^{17}$ m^{-3} for 7 mT. The reasons for this large discrepancy are not clear and must be further studied. It could be due to depletion of the neutral density, not taken into account in the simulation, to a larger effect of turbulence on the plasma density in the experiments, or to an inaccurate estimation of the charged particle losses to the end plates.

The plasma density in the simulation exhibits some instabilities as can be seen in Figure 2.9, which shows the 2D distribution of the plasma density at a given time of the simulation, for a magnetic field of 5 mT. The 2D distribution of the time averaged plasma density is shown for comparison in Figure 2.10. The instabilities seen in Fig. 2.9 are rotating over a time on the order of 5 μs. This corresponds to a rotation velocity around $4x10^{6}$ cm/s at a radius of 3 cm, i.e. close to the critical ionization velocity of hydrogen [31].

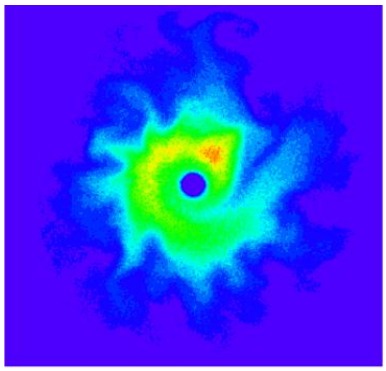

Figure 2.9: Distribution of the plasma density at a given time for B=5 mT, p=0.26Pa

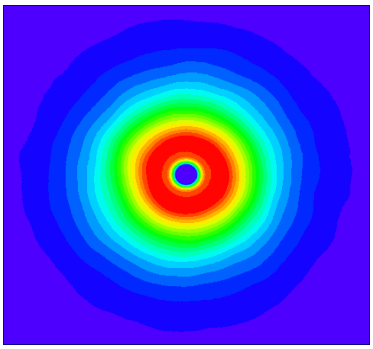

Figure 2.10: Time averaged distribution of the plasma density in the conditions of Fig. 3.2.

The large plasma density gradient that can be seen in the figures above is consistent with the experimental observations (see Fig. 2.3) and is due to the magnetic confinement along the field line and the fact that most of the ionization takes place (also because of the confinement) in a region of a few cm radius around the filament (the Larmor radius of 70 eV electrons in a 3 mT field is about 5 mm). The time averaged electron temperature for the magnetic fields is shown in Fig. 2.11. This temperature is on the order of 10 eV around the filament and drops to about 1 eV next to the wall.

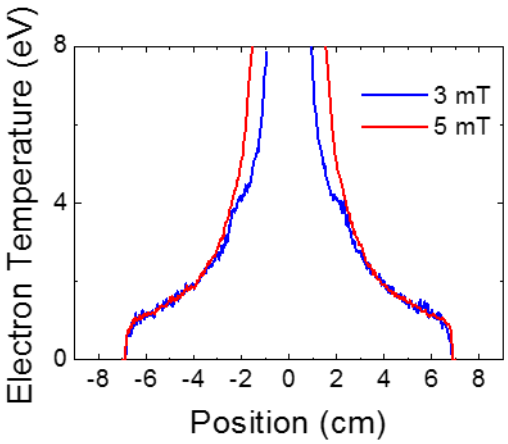

Figure 2.11: Radial distribution of the time averaged electron temperature.

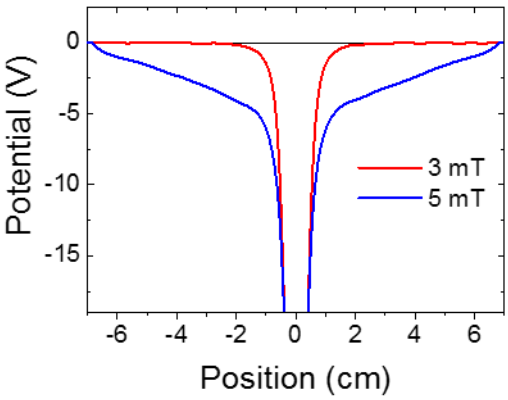

Figure 2.12: Radial distribution of the time averaged plasma potential.

The radial profile of the time averaged plasma potential in figure 2.12 shows that at a low magnetic field (3mT), the plasma bulk is equipotential (E=0V/cm), while at a higher B-field (5mT), a time averaged radial electric field of about 1 V/cm appears in the plasma. This is consistent with the Langmuir probe measurements in Cybele (see figure 2.5).

The results above have been extended to include negative ions in the simulations. The principal properties of the plasma are not strongly modified by the presence of negative ions. The rotating instabilities may however be less important in the presence of non-negligible densities of negative ions because of the resulting increase in conductivity (ions are much less magnetized than electrons). Work is in progress to quantify this effect and its consequences on the plasma properties.

Finally we note that a 2D fluid model (MAGNIS code) [32] that can describe a large range of conditions of ion magnetization (from non-magnetized to fully magnetized) has been developed at LAPLACE and compared with the TOKAM code of IRFM for conditions where ions are strongly magnetized [33]. This model is now being used together with the PIC MCC simulations to study the properties of the plasma in the Cybele source.

2.3 - Development of a helicon generator for Cybele (CRPP Laboratory)

The ability to obtain high plasma density with high ionisation rate and a much higher power efficiency than inductively-coupled plasma (ICP) sources makes helicon sources an interesting option as plasma source for Cybele. Since first experiments performed by Boswell [34], helicon sources have been extensively studied and they are proven to be very efficient for high-density (10^{12}-10^{13} cm^{-3}) plasma production with moderate injection power. Historically, they have found a wide range of applications, including semiconductor manufacturing and space-based thruster system. Recently, they have been considered for nuclear fusion applications and proven to be a very promising candidate as plasma generator for negative hydrogen ion sources for ITER [35]. In this context, helicon sources have the following advantages over traditional ICP generators: 1) reduced required RF power, leading to increased operational domain; 2) stable operation at low pressure (< 1 Pa), reducing negative ion losses by electron stripping; 3) lower electron temperatures, resulting in higher efficiency of negative ion production; 4) high degree of molecular dissociation in hydrogen plasmas.

In the framework of the collaboration between the CEA and the CRPP-EPFL, a 10kW helicon plasma generator will be implemented on Cybele and compared with the "ICP data base". Although a single 10kW helicon generator will probably not achieve the relevant plasma density required for NB sources for future fusion grade reactors, the 10kW helicon source is an intermediate step towards larger helicon powers, which will allow investigating the main technology and physics issues related to high power helicons.

As proposed by Chen and co-workers [36], the helicon wave excitation can be optimized by matching the field generated by the antenna to the expected helicon wave field. In standard helicon sources, this is obtained by using specially shaped antennas, such as the Nagoya III antenna [37], the paddle-shaped antenna [38], and helical antennas [39]. In the past years at CRPP, a new type of helicon source was developed, which is based on the concept of a resonant birdcage network antenna [40,41,42]. A birdcage resonant antenna is shown in Fig. 2.13 using a CAD drawing of the antenna specifically designed to fit on Cybele. The antenna is made of conducting parallel legs distributed around a dielectric tube in a cylindrical configuration. Each leg is connected at both ends to its closest neighbours by capacitors. This structure can be seen in a first approximation as a parallel arrangement of L, C lumped elements, and presents a set of resonant frequencies corresponding to the normal modes of the structure. When excited at one of its resonant frequencies a strong, azimuthally sinusoidal, distribution of current amplitude is generated in the antenna legs, all these currents being temporally in phase. The RF fields generated by these current distributions fit well the helicon wave field structure, thus resulting in an efficient excitation of helicon waves.

The birdcage helicon antenna was already shown to be very efficient in terms of helicon wave excitation for low RF power injection (<1 kW). Electron densities (from line integrated interferometric measurements) of ~5 10^{18} m^{-3} were obtained in a 10 cm discharge tube, with

argon at 1 Pa and for 300 W of power injection. It has also been shown that the birdcage resonator allowed many limitations inherent to conventional antenna designs to be overcome (pressure range for which helicon regimes can be sustained, use of high flux of electronegative gases, non-uniform static magnetic field). Furthermore, beside its ability to efficiently generate the helicon discharges, the resonant network has very interesting properties in terms of its input impedance. In fact, these antennas present large, purely real input impedance at the resonance, even when coupled to plasmas. In terms of impedance matching between the RF generator and its load this constitutes a major advantage with regard to conventional antennas, which present almost purely reactive impedances and are then strongly mismatched with the standard real 50 Ohms output impedance of the RF generators. The birdcage antenna design is therefore an ideal candidate for the negative ion generator for fusion applications.

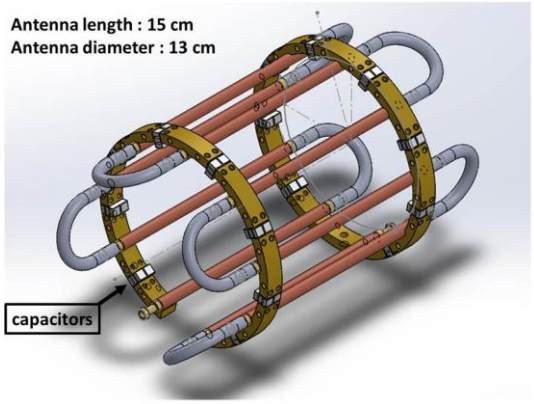

Figure 2.13: 9 leg cylindrical resonant network used for helicon excitation. The capacitors value is 3840pF to bring the m=1 resonance close to 13.56 MHz (with the screens). With regards to the closed configuration, the chosen open configuration allows a better control of the RF field polarization to be obtained.

A birdcage resonator able to withstand 10 kW RF power was designed and is presently under construction. The antenna diameter is 13 cm to fit with the Cybele source and the 15 cm long conducting parts are made of copper tubing to allow water cooling of the system. The capacitors are made of parallel arrangements of 6 high Q (quality factor) mica capacitors. The total individual capacitance of each arrangement (C= 3840pF) was chosen to obtain an m=1 resonance of the birdcage at 13.56 MHz. The choice of this frequency, besides being a standard in the industrial plasma field, is justified by the availability of a 15kW, 13.56MHz power supply at CRPP. In a first phase before the test on Cybele, the helicon source will be installed on a large cylindrical (diameter: 0.4 m, length: ~ 2 m) vacuum chamber at CRPP.

During the first period, the birdcage helicon antenna will be tested at CRPP. This investigation will focus on important issues in the application as NBI plasma sources (hydrogen gas, low magnetic field operation…). Particular care will be devoted to study the important thermo-mechanical response of the high RF power plasma source. Intensive plasma diagnostic measurements will be made on the 10 kW helicon source. First measurements will be performed using Langmuir probes, microwave interferometry, emission spectroscopy and

possibly also time-resolved emission spectroscopy, which might provide a deeper insight in the complex mechanism of plasma production associated with helicon waves. These studies will advance our understanding of the physics of helicon plasma sources and their application as plasma sources for NBI.

2.4 Development of Cs-free solutions for negative-ion production in Cybele (PIIM, LSPM laboratories):

The only up-to-date available scientific solution to reach the high D- negative-ion current required for fusion is the use of cesium. Studies conducted at IPP Garching on the ITER negative-ion source show that ITER requirements in terms of current density can be reached using this solution [43,44]. Cesium is injected in the negative-ion source and deposits on all surfaces in contact with the plasma. Deposition of cesium lowers the material work function and allows for high surface ionization efficiency upon impact of deuterium positive ions or atoms, and thus allows reaching high negative ion yields. Furthermore a huge number of negative-ions are created on the plasma grid, just nearby the extraction grid, in a region where the electron temperature is low (on the order of 1 eV). Therefore, the chances to extract the negative-ion before its destruction by electron collision are high. The cesium method can be used in the Cybele negative-ion source to produce negative-ions. However, drawbacks to the use of cesium have been identified. First, to obtain stable negative-ion currents over long shots, a continuous injection of cesium is required, leading to a high cesium consumption (~3 µg/s [45,46]). Second, cesium diffusion and pollution of the accelerator stage might cause parasitic beams and/or voltage breakdowns and imply a regular and restrictive maintenance in a nuclear environment. Therefore, a cesium-free solution would be highly valuable for future NBI devices. We are working on cesium-free solutions to produce negative-ions and we give here a brief introduction to this work.

Basically, negative-ions can be produced in the plasma volume through dissociative attachment of electrons on vibrationally excited molecules [47], or on surface through surface ionization process. It is improbable that the first solution could be used for a fusion source because it would require using higher pressure to increase the negative-ion yield, while lower pressure is required to minimize ion (D-) stripping in the accelerator channel. The second solution implies finding a material, other than cesium, which is able to strongly enhance surface ionization upon deuterium impact. Since the discovery of the cesium effect in 1971 [48,49], most of the studies have been focused on cesium, and the other low work function materials have been disregarded compared to cesium. Re-evaluating the use of other low-work function materials might be interesting. Apart from low work function metals, other materials with particular electronic properties might be interesting for negative-ion surface production. For instance, it has been shown in beam experiments that an enormous F- negative-ion yield can be obtained using covalent crystal (LiF) [50]. With the same material a rather high H^- ion yield (7.5%) has been obtained [51]. However, the chosen surface must not only enhance negative-ion surface production, but also handle the plasma exposure, be deposited on a metallic grid… Diamond which presens a negative electron

affinity (conduction band above the vacuum level) is an attractive material. The negative electron affinity would almost suppress electron detachment from the negative-ion (once the negative-ion formed, the electrons cannot detach back towards the material since the affinity level is not in resonance with any other level). Furthermore, diamond has outstanding thermal and mechanical properties (thermal conductivity of about 1800 $Wm^{-1} K^{-1}$, five times that of copper), it exhibits a much higher resistance to hydrogen plasmas than graphite, and can be deposited on metals, in particular molybdenum. In order to study negative-ion surface production in cesium-free plasmas, and in particular to study various layers of diamond materials, a dedicated experiment has been designed at PIIM laboratory [52-58]. The aim is to evaluate and optimize alternative solutions to caesium prior to testing them in the Siphore negative-ion source.

Figure 2.14 shows the measurement of the negative-ion energy distribution function from which it is possible to infer much information on the surface production mechanisms [53, 56, 57]. The area below the distribution function gives the relative negative-ion yield. It is not possible to perform an absolute yield measurement using this method unless a calibration with another diagnostic is carried out. At the moment, all the yields are relative and compared to that of HOPG (Highly Oriented Pyrolitic Graphite) which has proven to efficiently enhance the negative ion surface production. Yields on HOPG are for instance 1000 times higher than on copper or molybdenum and 10 times higher than on stainless steel. It has shown comparable yields at room temperature with a molybdenum sample implanted with a low-dose of cesium [78].

It has been shown that the extraction efficiency is higher for ions created at low energy and close to the normal to the sample surface, leading to a preferential measurements of ions created via sputtering mechanism (an adsorbed atom is sputtered as a negative ion) comparing to backscattering mechanism (an incoming ion is dissociated at impact and one of the fragment is backscattered as a negative ion) for which the mean energy and mean outgoing angle are higher.

The figure 2.15 presents yield measurements. Several carbon materials (in particular, several diamond layers) have been compared. Microcrystalline Boron Doped Diamond (MBDD) and microcrystalline non doped diamond (MD) as well as Nano-Crystalline non doped Diamond (NCD) layers have been tested, all of them having been deposited at LSPM laboratory, partner of the present project. Apart from diamond, HOPG, CFC (Carbon Fibre Composites used in the past as carbon tiles for tokamaks, here the C/C composite Sepcarb N11® has been employed). The yields have been measured at different surface temperatures with the sample normal to the mass spectrometer axis, and it has been checked that this measurement was representative of the yield at any angle. The striking point on this graph is the different behavior between the diamond group of materials and the other carbon layers. While on carbon layers the yield mostly decreases with temperature, the yield on diamonds at first increases with temperature, reaches a maximum around 400-500°C and then decreases. There is on the average (depending on experimental conditions) an increase of the yield by a factor of 3-5 compared to room temperature. Raman measurements have been performed after plasma exposure for some of these materials [55,58]. The yield maximum observed for diamond materials has been attributed to electronic properties

of the top surface that are favorable to surface ionization. These electronic properties are tuned by the sp3/sp2 ratio and by the hydrogen percentage. It is thus believed that there is room for optimization, and that diamond layers and/or defective diamond layers are promising candidates for negative-ion enhancer materials in hydrogen plasmas. Let us note that diamond has already proven to be efficient for H^- production in beam experiments, showing some yields on the order of several percent (5.5%)[59]. Diamond-like Carbon have even been chosen as a converter material for the detection of the low-energy heliospheric neutral atoms from 0.01 to 2 keV, for the mission of the satellite IBEX launched in 2008 [60]. Yields as high as 6% have been reported [61,62]. However, unless in the present study, none of these materials have been evaluated as converter materials under plasma exposure. The future work aims for better definition of the key surface state parameters leading to the high surface ionization efficiency. The diamond crystalline orientation will be studied using several kinds of diamond monocrystals, the doping influence will be studied using boron and nitrogen as dopants…

Figure 2.14: Negative ion yield versus surface temperature in low-pressure (2 Pa) deuterium plasma (RF power 20W). MBDD, MD, and NCD, stand for Microcrystalline Boron Doped Diamond (MBDD), microcrystalline non doped diamond (MD), and Nano-Crystalline non doped Diamond (NCD). HOPG, CFC and TaC stand for Highly Oriented Pyrolitic Graphite (HOPG), Carbon Fiber Composites (CFC) and tetrahedral amorphous carbon (taC).

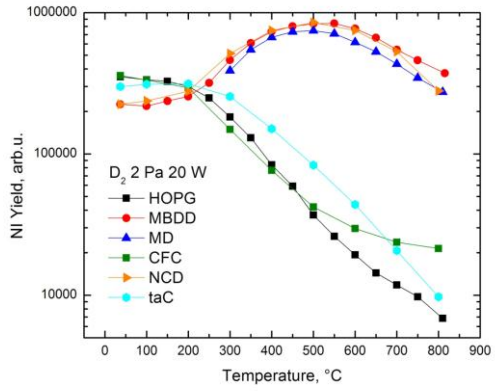

Figure 2.14: Negative ion yield versus surface temperature in low-pressure (2 Pa) deuterium plasma (RF power 20W). MBDD, MD, and NCD, stand for Microcrystalline Boron Doped Diamond (MBDD), microcrystalline non doped diamond (MD), and Nano-Crystalline non doped Diamond (NCD). HOPG, CFC and TaC stand for Highly Oriented Pyrolitic Graphite (HOPG), Carbon Fiber Composites (CFC) and tetrahedral amorphous carbon (taC)

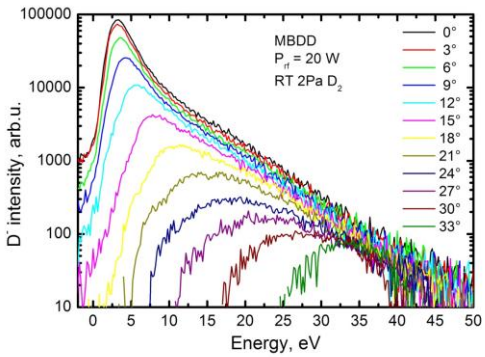

Figure 2.15: Negative-ion energy distribution functions measured on MBDD in deuterium plasma (2 Pa, 20W) with the sample set at different angles with respect to the mass spectrometer axis (0 stands for the normal to the sample surface aligned with the mass spectrometer axis).

3-ION BEAM ACCELERATOR

3.1- Siphore accelerator design and simulation (IRFM, NRC)

The interaction of the photon beam with the ion beam has to be maximized by a specific design and aspect ratio of the beam line; for this purpose, the intra-cavity photon beam must cross the ion beam several times to cover its width. A full overlap of the D^- beam can be achieved with a thin laminar D^- ion beam of width 3 to 6 cm in the photo-detachment area, and a three (or four) -times refolding cavity with an intra-cavity photon beam diameter of 2 cm (see figures 1.1 and 1.2). We suppose that the negative ions are extracted from a thin and long ion source 3m high and 15 cm wide, which produces a uniform D^- density current of $J_{D^-} = 250$ A/m^2 (same range as the ITER ion source) over the extraction surface.

On the front face of the ion source, the accelerator will have to extract and shape the D^- into a thin laminar beam (see figure 1.2) which will be post-accelerated at high energy (1 or 2 MeV). The main goal of the accelerator concept is to provide an intense pure D^- low diverging ion beam (ribbon shaped) in the photo-detachment region. For this purpose, the pre-accelerating grids have a transverse curvature radius (see figures 3.1 and 3.2) in order to merge and focus the beamlets in a single macro beam sheet in the post-acceleration stage (see figure 1.2).

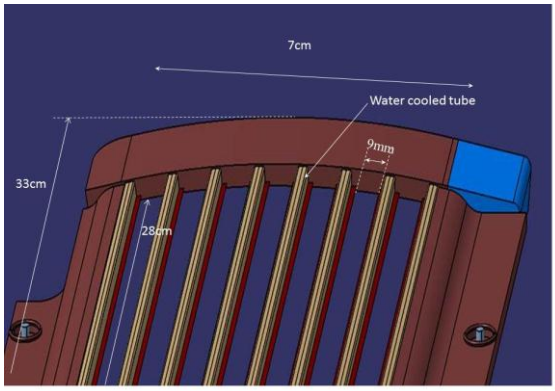

Figure 3.1: Engineering drawing (front view) of a pre-accelerating grid.

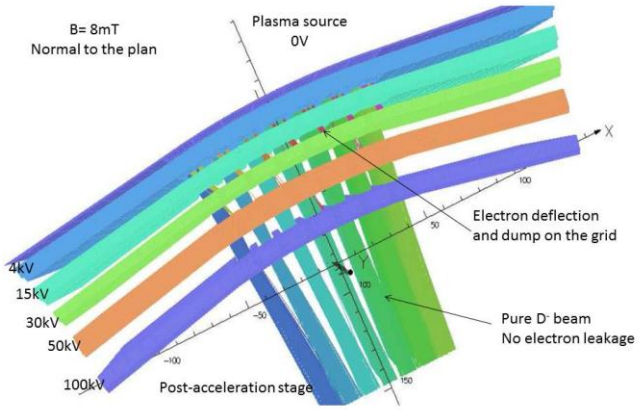

Figure 3.2: 3D simulation of the 100keV pre-accelerator

Moreover, the stray electrons, i.e., the co-extracted electrons with the D^- and the stripped electrons, in the pre-accelerating stage have to be efficiently suppressed. For this purpose, they will be deflected out from the ion beam and dumped onto the grid metal surfaces by a vertical magnetic field diffusing from the ion source (ranging around 8mT); the grids do not contain any

permanent magnets. In figure 3.1, we note that instead of cylindrical beamlets as used on the ITER NBI system, the grids are based on slot apertures, each slot is 0.9cm wide and 28cm height. Each grid contains seven adjacent slots leading to a high grid (accelerator) transparency close to 50%. The D^- current extracted by one grid is estimated to be 4.4 A (supposing $J_{D^-} = 250A/m^2$ on the source level). The entire accelerator extraction surface which faces the ion source will consist of several grids (3 grids per meter leading to about 13 A of D^- per meter height) set up along the source vertical axis and spatially oriented in order to focus the neutral beam 10m downstream within the duct of the Tokamak plasma chamber. The overall extracted D^- current from a 3m height ion source ranges around 36A.

On figure 3.3 is depicted a rough estimate of the pressure profile within the pre-accelerator stage assuming 0.3 Pa of source pressure and a gas temperature of 300K. The stripping losses within the pre-accelerating channel is estimated to be 18%, leading to 30A of D^- at the pre-accelerator exit (in the post-acceleration stage). The stripping losses within the post-acceleration stage are neglected due to the low background pressure in the vacuum tank and the drop of the stripping cross sections for an energy higher than 10keV (see Fig. 3.4).

For instance, for 36 A D^- beams extracted from the source, there are 9 units of grids on top of each other. For a source pressure of 0.3Pa, the gas flow rate in the pre-accelerator is 1000 Pa l/s. Supposing a background tank pressure of 10 mPa, the required pumping speed is $S= 10^5$ l/s and the stripping losses in the post-acceleration gap (to 1MeV) amounts to only 3%. It is clear that photoneutralization leads to an important economy of the pumping system; the pumping speed of the ITER-NBI system based on gas neutralizer being $5\ 10^6$ l/s [6] .

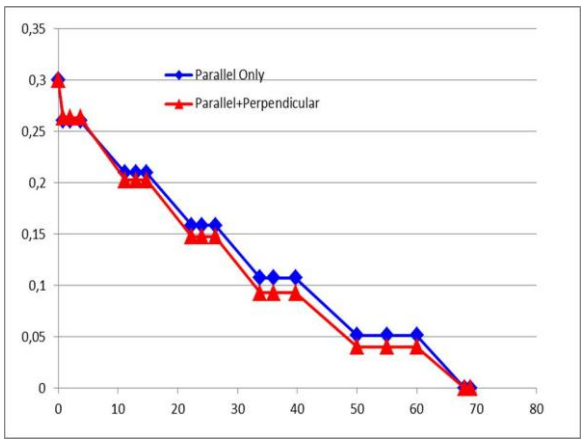

Figure 3.3: estimate of the pressure profile within the pre-accelerator stage; we note that the perpendicular conductance appears to be much smaller than the parallel conductance.

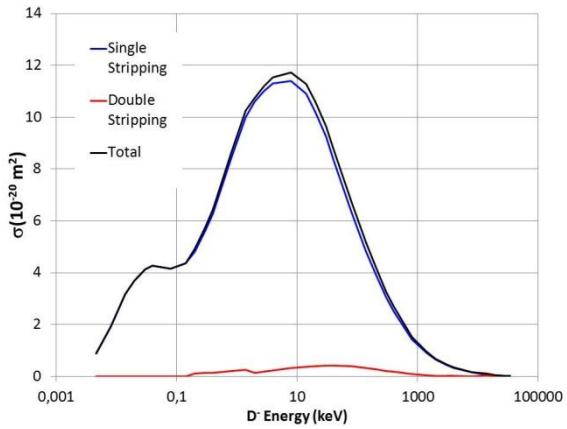

Figure 3.4: Stripping cross sections for deuterium beam as function of the beam energy

Figures 3.2 and 3.5 (same simulation as figure 3.2 with grids 2, 3, 4, 5, 6 masked) show a 3D simulation with the Opera-Scala code [63] of the electron suppression (deflection) in the 100 keV Siphore pre-accelerator by the magnetic field diffusing from the ion source.We note that the electron suppression is complete (no electron leakage in the post-acceleration stage), the major part of the co-extracted electrons are dumped on the first three grids (at 5, 15 and 30kV) for a magnetic field of 8mT. With the slot geometry, the thermal load is uniformly distributed along the tube height.

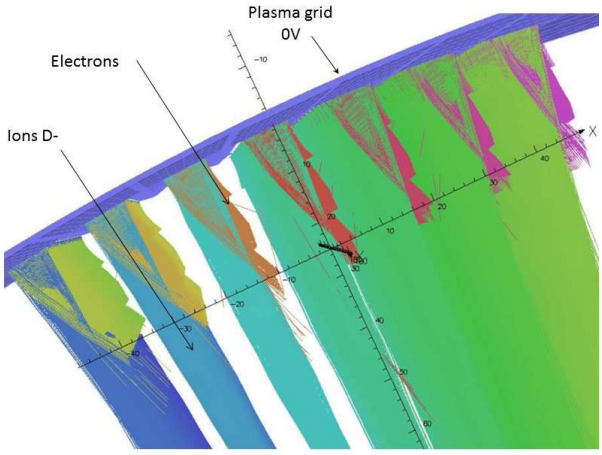

Figure 3.5 Same simulation as figure 3.2 with grids 2, 3, 4, 5, 6 masked.

Assuming one co-extracted electron per D^- from the plasma source (i.e., ~4.4A of co-extracted electrons per grid), the thermal load (thermal power) on the downstream pre-accelerator grids is estimated by the electron current dumped by each grid (obtained from simulations):

G_2 at 5kV, P_{G2} = 6kW; G_3 at 15kV, P_{G3}= 40 kW, G_4 at 30kV, P_{G4}= 12 kW

Thermo-mechanical simulation of the grids has been done using the Ansys software. Simulations show that water cavitation occurs in the tubes when the thermal load is higher than 80 kW (per grid).

In parallel to the simulation with Opera, 3D simulation of the electron trajectories in this 100keV accelerating channel have been performed using an in-house written code similar to the 3D EAMCC code [64]. The specific role of these codes is to take into account of the atomic processes occurring within the accelerating channel (interaction of particles with gas and metal surface), mainly the stripping reactions of negative ion collisions with the background gas and the secondary electron emission of the grid metal surfaces due to particle bombardment.

Figure 3.6 shows the 3D trajectories of the co-extracted electrons with a magnetic field of 6 mT. We can note that the co-extracted electrons are deflected later (due to a lower Larmor radius), and that the thermal load is higher on grids at 15 and 30kV. These simulations indicate that the optimum magnetic field for an efficient (complete) electron suppression ranges around 8mT. Figure 3.7 shows the 3D trajectories of the stripped electrons emitted within the

accelerating channel; we note that they are intercepted by the last two grids (at 50 and 100 kV) and the suppression is nearly complete.

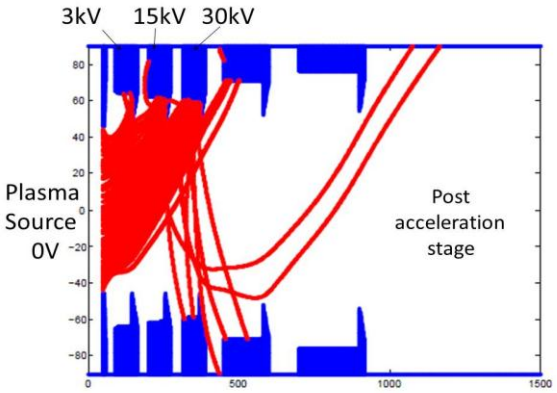

Figure 3.6: 3D trajectories of the co-electron in one pre-accelerating channel (top view of one slot) for a uniform magnetic field (normal to the plan of the figure) of 6 mT.

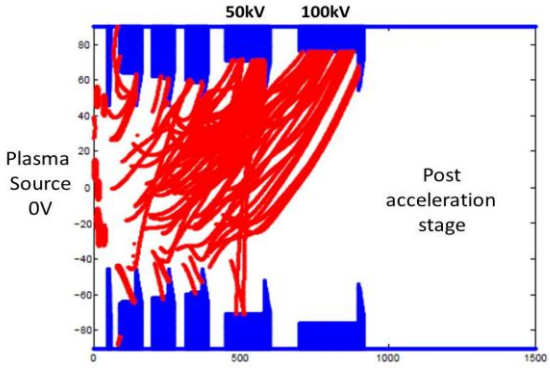

Figure 3.7: 3D trajectories of the stripped electron in one pre-accelerating channel for a magnetic field of 6 mT.

The D^- beam emittance diagram at the exit of the pre-accelerator (see figure 3.2) for a uniform magnetic field intensity of 8 mT is shown on figure 3.8; we note an overall ion beam deflection of 20 mrad, which can be canceled by a lateral aperture displacement (δ=1.1 mm) of the last grid (at 100 kV) which transversally steers the ion beam in the opposite direction (see Fig. 5.9).

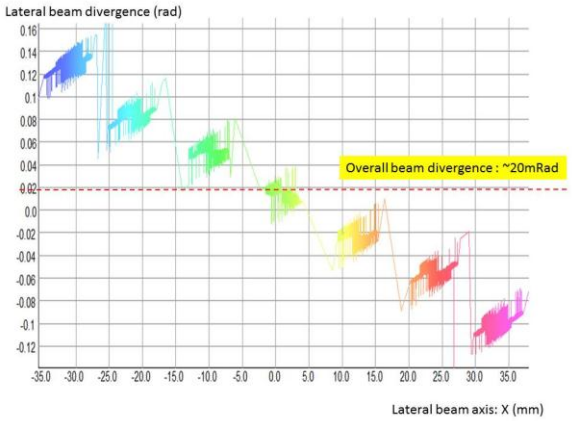

Figure 3.8: D^- beam emittance diagram at the pre-accelerator exit for a magnetic field of 8mT.

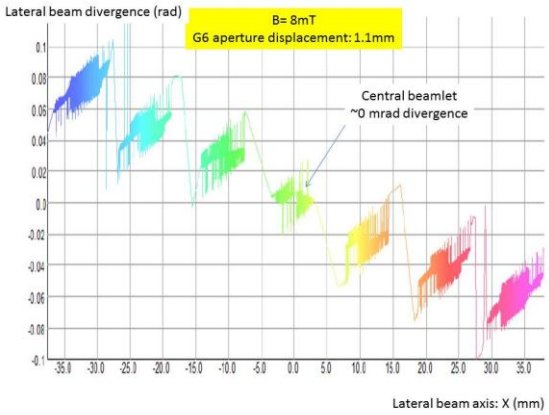

Figure 3.9: D^- beam emittance diagram at the pre-accelerator exit for a magnetic field of 8mT with beam steering by an aperture displacement of 1.1 mm in the 100 kV grid

The ion beam is then post-accelerated in a single gap up to 1 MeV or via a tandem configuration to 2MeV with the ion source polarized at -1MV, the photoneutralizer at +1MV with an intermediate grounded electrode (see Fig. 3.10).

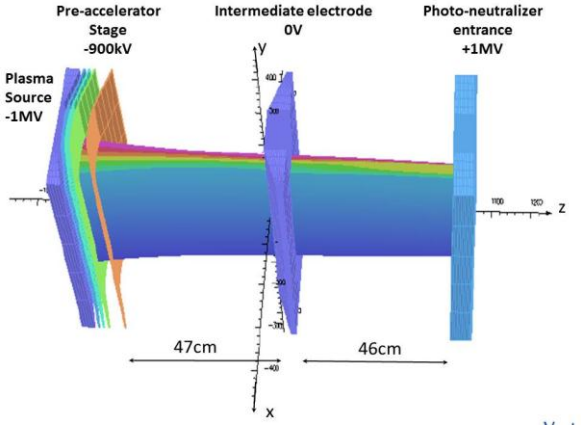

Figure 3.10: 3D simulation of the 2MeV D^- beam ; the D^- current in the post-acceleration stage is 3.7A.

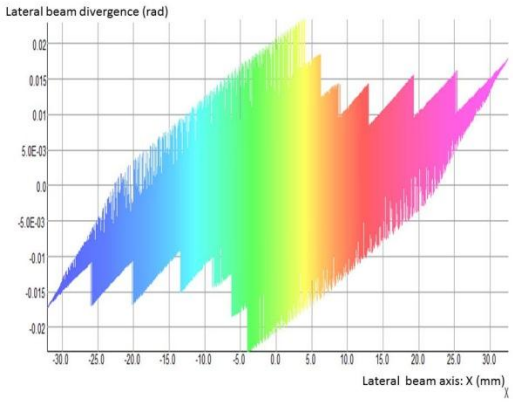

Figure 3.11: 2MeV beam emittance diagram at the photo-neutralizer entrance.

The 2MeV beam emittance diagram (see Fig. 3.11) at the photoneutralizer entrance indicates an overall beam width of 6cm with a divergence of 15mrad for the central beamlets, and a higher divergence (~20mrad) for the two external beamlets (slots) of the grid.

3.2 - Preliminary modelling of the 1MeV D^- beam in the photoneutralizer (LPGP Laboratory)

The photoneutralization of the D^- high energy negative ion beam was primarily modelled, inside a 'vacuum' neutralizer system, following the Siphore concept described in the Introduction (Fig. 1.1). The meaning of the word 'vacuum' represents the very low level of the residual gas pressure filling the volume between neutralizer plates. Hence, the energetic beam particles interact exclusively with the laser photons trapped in each Fabry-Perot cavity, and the eventual development of a secondary plasma by the residual gas ionization is highly improbable. However, the 1 MeV D^- beam stripping due to the interaction with the D_2 gas has been extensively studied for the ITER-like neutralizer [65]. The main conclusions of the gas neutralization are (i) the very efficient compensation of the D^- beam space charge by the secondary plasma developed due to the ionization of the gas molecules by the energetic beam particles; (ii) the neutralization efficiency can reach the theoretical value, i.e., ~56% conversion of D^- in D°. Therefore, this section aims to present the first numerical simulations for the case where the D^- beam is only neutralized by photons, which is the novelty of Siphore concept.

Let us underline that the gas neutralization leads not only to one electron striping but also to double stripping (producing D^+), while the photons absorption by the negative ions leads necessarily to the extra-electron detachment, and the double stripping is unworkable (the photons energy hν being much below the ionization energy of deuterium).

Modelling background:

Briefly, ONAC (Orsay Negative ion ACcelerator) 3D code [66] has been adapted to describe Siphore photoneutralizer parameters such as plate potential, geometry and beam features given in Fig. 1.2. ONAC code developed at LPGP is based on the Particle-in-Cell (PIC) approach and it takes into account the space-charge of the beam solving 3D Poisson's equation. The beam particles are thus moved in the 3D up-dated electric field until the steady-state is reached. Moreover, it can take into account the particle kinetics inside the simulation volume treated by Monte Carlo Collision (MCC) algorithm. In this sense, ONAC is self-consistent as the other two 3D codes developed at LPGP to simulate other components of the NBI, namely ONIX (Orsay Negative Ion eXtraction) [67,68,69,70], which simulates the extraction of negative ion from the plasma source, and OBI (Orsay Beam Injector), which simulates the gas neutralization [65].

ONAC was developed from the very beginning to simulate the ion beam transport (negative or positive ions) for NBI systems. The input geometry of acceleration electrodes can be easily modified due to the object oriented implementation. In addition, all the 3D codes have been parallelized using Massage Passing Interface (MPI) protocol.

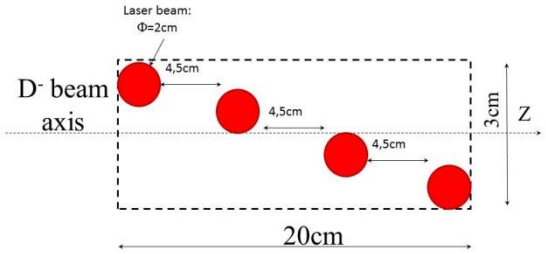

Figure 3.12: Simulation domain with one Fabry-Perot Cavity (50% of neutralization rate) inspired by the photon trajectories depicted in Fig. 1.2. The cavity length is 20cm.

If the four vertical paths of the laser beam (20 mm diameter) are all in one plane (blue line), than proceeding to a little tilt of this plane with respect to the D^- beam axis (Fig. 3.12), it becomes possible to cover a vertical space trench of 3 to 6cm width, the same as the waist of the focused NI beam.

Test-case photo-neutralizer with two cavities of 40% neutralization efficiency each : The first simulations have been performed assuming a neutralizer with two identical Fabry-Perot Cavities (FPC) detailed in Fig. 3.12, separated by 20 cm, and placed at 20 cm from each end. The photo-detachment rate is taken 40% for each photon beam cavity.

The 3D ONAC code has been adapted in order to fit with this photoneutralizer test-case geometry, consisting of two parallel plates separated by 5 cm and equipotentially polarized. The D^- particles are injected with an energy of 1 MeV and the beam is 3 cm width with an initial divergence of 3 mrad. The beam height is taken 10 cm, representing 30 A of D^- for a linear beam of 3 m height (see Fig. 1.1).

This numerical simulation shows that the neutralization efficiency is very close to the expected theoretical value of 76% D° production for this test-case. The remaining energetic beam particles (D^-) conserve their charge (remember that NI can be destroyed only if they interact with photons) and the effect of the beam space charge is shown in Fig. 3.14, when the steady-state is reached, after about 100 ns, and the beam parameters are stable.

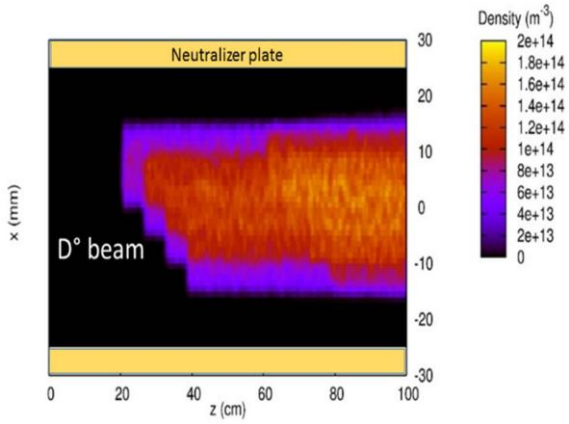

Figure 3.13: D° beam propagation through the neutralizer cell; represented in 2D (x,z) cross section for two FPC of 40% neutralization efficiency each.

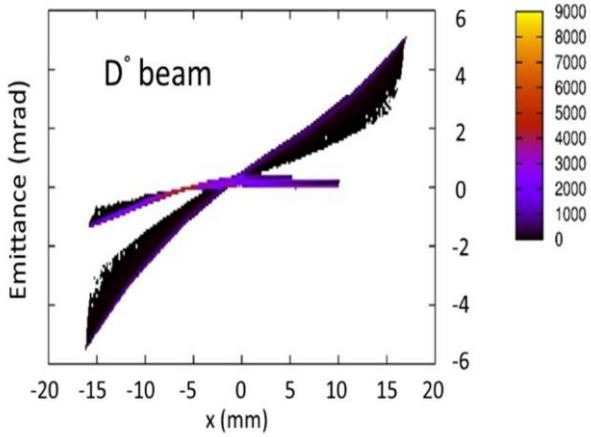

Figure 3.14: Beam emittance diagram at the neutralizer exit for the neutral beam corresponding to the Fig. 3.13.

The Fig. 3.14 demonstrates that the very good efficiency of the neutralizer, especially in the central part of the beam, around the symmetry axis (x=0). Only a few D^- peripheral ions are deflected off-axis because they can cross the first FPC preserving their charge, and are subject to the Coulombian repulsion in the transverse direction. As the photo-neutralization process does not affect the particle momentum, than the D° produced in the second FPC will continue with the small deflecting angle attained in the free space between the two laser cavities. This is visible on the emittance diagram shown in Fig. 3.14, which clearly presents two shapes. At the exit of the first FPC, the divergence keeps close to its initial value (3mrad) while the divergence has increase up to 6mrad after the second FPC.

Another test-case has been run with 60% photo-neutralization efficiency, assuming a higher laser power trapped in the cavity. In this case the total neutralization is even closer to the theoretical value of 84%. Concerning the D° beam emittance at the exit plane of the neutralizer, it

is shown in Fig. 3.15. Comparing the emittances represented in Fig. 3.14 and 3.15, it comes out that increasing the laser power in the cavities, reduces the beam expansion (the beam divergence) by space charge effect.

Also, one can see the signature of each laser beam of the first cavity (red dots on Fig. 3.12). Hence, the part of the D° beam particle neutralized first (by the top-left beam; Fig. 5.12) conserve an excellent emittance, centered on 0 mrad and with x lying from 0 to 15 mm. The second path of the laser beam in the cavity lead to a slightly spread beam visible on the emittance diagram (Fig. 3.15) at about 0.2 mrad and with x lying from -5 to 10 mm. The last (fourth) laser beam photodetaching the D^- beam leads to the highest divergence of D° with -1 mrad and x lying from -15 to 0 mm.

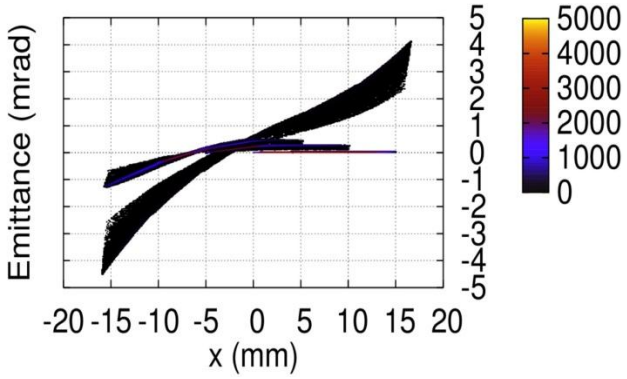

Figure 3.15: Beam emittance diagram at the neutralizer exit for the neutral beam produced by two FPC of 60% neutralization efficiency each.

As a partial conclusion of this studied test-case supposing no residual gas in the neutralizer cell, the beam induced divergence in the photoneutralizer decreases with increasing the photon power in the FPC. The simulations of the secondary plasma formation which would cancel the beam space charge (the beam expansion in the photoneutralizer cell) with the residual gas (or a minor gas injection) in the photoneutralizer is part of further research combining OBI 3 [65] and ONAC.

3-3) Energy recovery system (IRFM, NRC)

The concept of the energy recovery is based on the conservative property of the Coulomb (electrostatic) force; the residual negative ions at the neutralizer exit which are at the high energy (1 or 2MeV) are decelerated down to a low energy (~100keV) and collected onto the recovery electrode to a potential close to the source potential, i.e., 100kV for a 1MeV beam (see Fig. 1.3), or -900kV for a 2MeV beam (see Fig. 1.5).

In order to prevent the retro-acceleration of the secondary electrons emitted by the ion bombardment (on the recovery surface) towards the photoneutralizer at +1MV, the negative ions have to be collected within the recovery cell where a local vertical magnetic field ranging around 20mT deflects the negative ions towards the recovery surface. Figure 3.16 shows a 3D simulation of the 2MeV beam recovery: the remaining negative ions (4A of D^-, J_D-= 40A/m^2) at

photoneutralizer exit are decelerated in two stages, from +1MV to 0V and to -900kV. They enter the recovery cell with an energy close to 100keV where they are transversally deflected by a vertical magnetic field (~20mT) and dumped onto the surface. The magnetic field is generated by two lateral coils similar to the Cybele ones (see Fig. 2.1-b) with an iron core which surrounds the recovery cell.

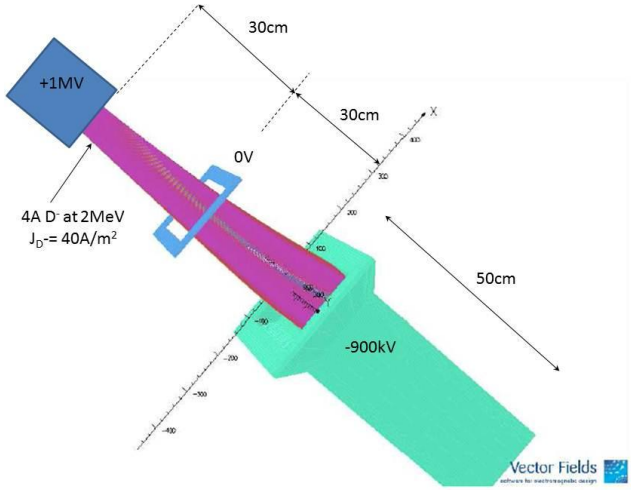

Figure 3.16: 3D simulation of the 2MeV beam recovery; the magnetic field is generated by lateral coils implemented onto the recovery cell (the coils are not represented on the figure), the field intensity is 23mT. The D^- beam is entirely collected and dumped within the recovery cell.

4- R&D IN PHOTONEUTRALIZATION

4.1 Photo-detachment physics (LAC Laboratory)

The photoneutralisation-based neutral beam systems concept relies on the elementary process of photodetachment of a negative ion. A photon with an energy hν large enough can be absorbed by a D^- ion to make a detachment reaction occur:

$$D^- + h\nu \rightarrow D^0 + e^-.$$

The isotopic shift being negligible, everything that we know about H^- photodetachment can be applied to predict how D^- photodetachment will work in a photodetachment-based high energy neutral (D^0) beam injector.

There has been no mystery, for the last fifty years, that H^- photodetachment is not a very effective process. The photodetachment cross-section σ, which, when multiplied by the light flux Φ expressed in photons per s and per m^2, gives the photodetachment probability per unit of time, is only a few 10^{-21} m^2. This is very low when compared to the few 10^{-12} m^2 possibly reached by the cross-section of an atom at the resonance of an electric dipole transition (such as a Na atom illuminated by yellow light at λ=589 nm), but photodetachment is a non-resonant process. This has, nevertheless, a positive counterpart: the wavelength is not critical, and the wavelength

λ=1064 nm of a Nd:YAG or Nd:YVO_4 laser, sitting close to the cross-section maximum, appears very convenient.

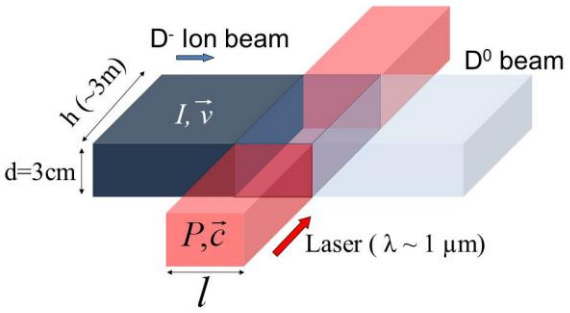

Figure 4.1: Ion-photon interaction region

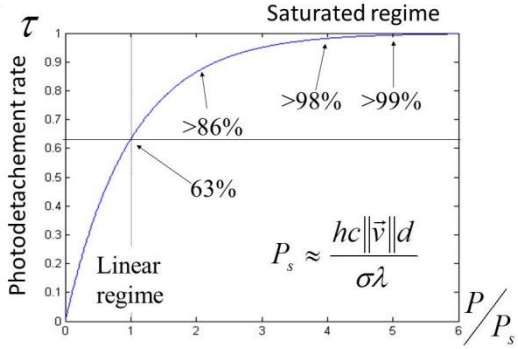

Figure 4.2: Photodetachment rate as a function of the relative photon power

Another consequence of the non-resonant character of the photodetachment process is that total detachment, i.e. 100% neutralization of the sample, cannot be reached but asymptotically with infinite power. The probability per unit of time of the photodetachment process being always the same, the population of ions illuminated by a laser beam decreases exponentially, without ever being reduced to zero (see Fig. 4.2). Yet after one "period" of the exponential decrease, it will already be reduced by a factor 1/e, which corresponds, as for the photodetachment process, to a 63 % efficiency. 95% efficiency is reached after only three "periods".

The value of the cross-section σ is a central parameter for dimensioning a photoneutralizer. The photon flux Φ necessary to have ions, of velocity v, reach one-period photodetachment decay rate of 63 % is just $\Phi=vd/\sigma$, where d is the common transverse dimension of the overlapping ion and laser beams (see Fig. 4.1).

Hence the necessity of making one transverse dimension of the ion beam as small as possible; d=3 cm appears a good compromise, for an ion beam of 30 A. With $\sigma\approx4.10^{-21}$ m^2 and a velocity v=9.8 10^6m/s (1 MeV of kinetic energy, 2 MeV would increase it by√2), the required flux is just 7.3 10^{25} ph $m^{-2}s^{-1}$, i.e., at the wavelength 1064 nm, of the order of 10 MW, which can be reached by three- or four-times refolding of a 3 MW light beam (see Fig. 1.1).

Paradoxically, before we began the project, the photodetachment cross-section of H^- had never been measured with a laser. This is not to say that measurements carried out with classical light sources are not valid for laser excitation, but, as a matter of fact, the last measurement of σ dated back to 1976 [71] and relied on the analysis of the radiation emitted by a hydrogen plasma.

In 2013 one of our laboratories performed a laser photodetachment experiment that relied on the saturation of the photodetachment of an H^- beam by a pulsed Nd:YAG laser to measure the cross-section without having to calibrate the ion current nor the detection efficiency. Provided the detection signal remains a linear function of the number of actual detachment events, either relying on the supposed Gaussian profile of the laser beam or using the saturation to set a probability scale of the detection signal, the cross-section was found to be slightly larger than what most theoretical calculations had predicted, namely 4.5(6) 10^{-21} m^2 instead of 3.6(1) 10^{-21} m^2 [9,10,11].

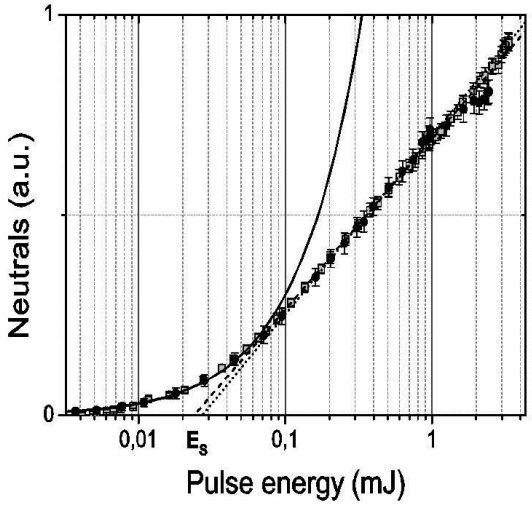

Figure 4.3: the (unnormalized) number of photodetachment-produced H_0 atoms as a function of the laser pulse energy in the pulsed-detachment experiment at LAC. Using a lin vs. log scale, one can easily extrapolate down to the saturation energy E_S, the value of which is enough to determine the photodetachment cross-section, provided one has a reliable value of the laser waist and laser pulse duration.

Given that the majority of theoretical calculations have predicted the lower value, this result may cause some controversy (even though some calculations still predict a higher value). The larger value would actually be only good news. The order of magnitude remains the same, anyway; photodetachment-based neutral beam injectors can be designed relying on a 4 10^{-21} m^2 cross-section value. Having a slightly lower or higher cross-section is an uncertainty much less significant than all the other uncertainties concerning the implementation of a medium-finesse cavity on an ion beam. One can even imagine that measuring the actual Q-factor of the cavity will remain so difficult (for any power measurement inside the cavity would immediately decrease its finesse substantially) that even the final full-scale experiment will probably not make it possible to decide whether the cross-section is closer to 3.6, 4 or 4.5 10^{-21} m^2.

Preliminary cavity experiments at LAC laboratory:

Amplifying the flux of a continuous-wave (CW) laser in an optical cavity, even with finesses larger than 10,000 and amplification factors of more than 3,000, is an everyday experiment. The special difficulties arising in the development of the photodetachment-based neutral beam generator are i) several MW of light flux are required (whereas high-finesse cavities are usually made for metrology purposes, i.e. at very low light fluxes) ii) this has to be implemented in a photodetachment machine, i.e. with an ion beam across the optical cavity, and

no longer in a pure optics experiment. Setting an optical cavity on an ion beam, in order to investigate the special problems due to that environment, is under development in the laboratory.

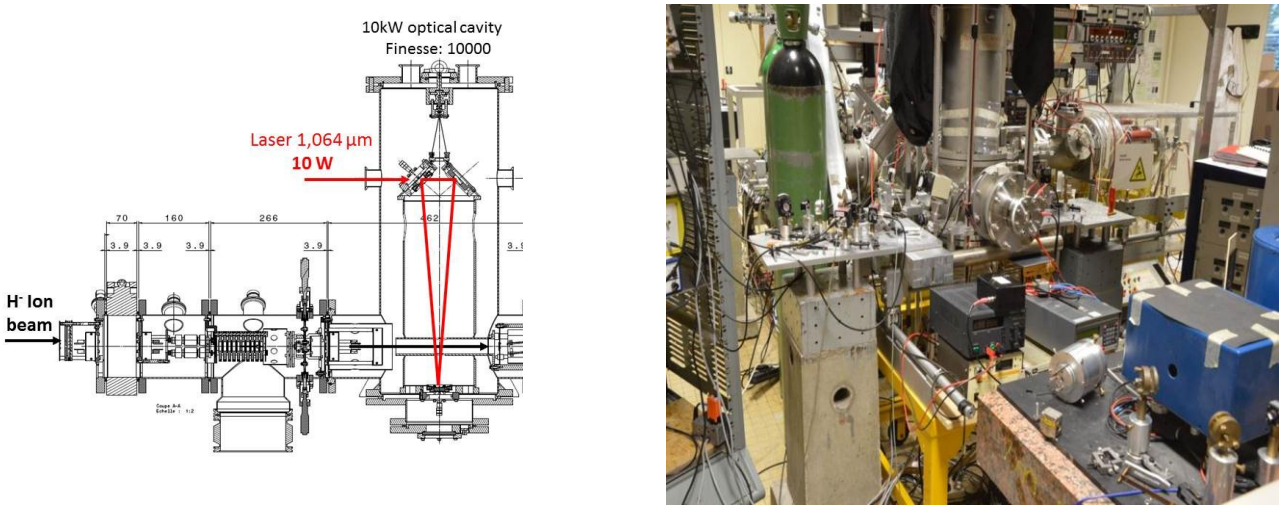

Figure 4.4: The photodetachment experiment at LAC equipped for intra-cavity photodetachment studies; (left): Engineering drawing of the experiment; (right): Photograph of the testbed

Enhancing photodetachment by laser amplification in an optical cavity is not a completely new experiment either. Intra-cavity photodetachment was used in some atomic or molecular physics experiments, either to produce neutral beams for collisional studies [72] or to enhance the photoelectron signal [73]. This was still far from saturation however, the photodetachment efficiency in these experiments never exceeded a few %. In order to get familiar with the technical problems encountered when mounting a higher-finesse optical cavity around a negative ion beam, we transformed the photodetachment microscope, in operation at LAC since 1996, to use optical-cavity amplification and began intra cavity photodetachment experiments (see Fig. 4.4).

Nearly total photodetachment of H^- will not be demonstrated in the photodetachment microscope (even though photodetachment microscopy of H^- would be of great interest) but on another line set on the negative ion machine, in a vacuum chamber specially built to accommodate a suspended optical cavity.

Suspension of the optical cavity as a whole should have the advantage of a much better stability for its length. In addition, contrary to the photodetachment microscopy case, the absolute wavelength of the injected laser is not a critical parameter, which makes it possible, in order to

maintain the laser-cavity resonance, to have the laser wavelength follow the cavity length fluctuations, instead of implementing a cavity-length servo-locking procedure. Both methods will be tested in 2015.

4.2 Study of a high power (3MW range) Fabry-Perot cavity (ARTEMIS laboratory)

As mentioned above, the requested photon power for 50% neutralization rate of an ion beam (D^-) at 1 MeV energy lies around 3MW with a photon beam width of 2cm. Such high photon power could be reached by using a low power laser beam which is retro-reflected several thousands of times (~10000) within Fabry Perot cavity.

As shown on figure 4.5, the 30A D^- beam at 1MeV is supposed to be a 3 cm wide slab vertically extruded over 3m height, it is crossed by the intra-cavity photon flux. The cavity design consists in a four times refolded cavity with arms of 25m long leading to a 100M long intracavity roundtrip. The intra-cavity photon beam width is 2cm with less than 10 % variation along the cavity, leading to a good optical stability which is less sensitive to misalignments. Thus, mirrors can be set up far away from the plasma environment in a separated vessel in which a differential high vacuum can be guaranteed (see Fig. 1.5 and 4.5).

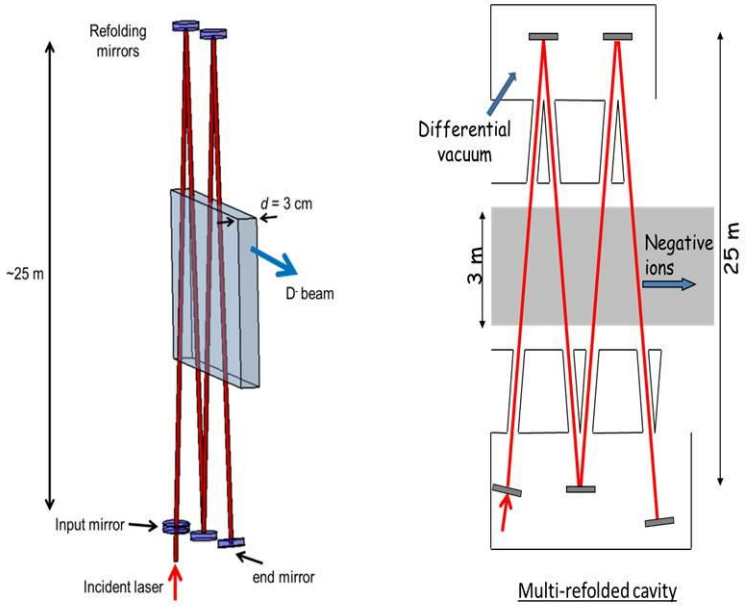

Figure 4.5: Geometry of the refolded optical cavity

High intra-cavity power (P_{int}) can be reached either by increasing the number of round trips, ie, the cavity finesse (F), or by increasing the impinging laser power (P_0). The intra-cavity power is limited by the intra-cavity losses (Λ) over one roundtrip.

Eq.2: $P_{int} = S * P_0$

with S the enhancement factor:

$$S = \frac{2F}{\pi\left(1 + \frac{\Lambda F}{2\pi}\right)^2}$$

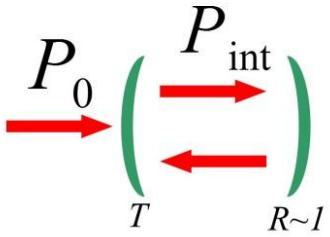

The losses Λ over one round trip in the cavity result from different sources:

-i) the scattering losses on the mirrors ~10 ppm per mirror for a beam width of 2 cm, i.e., 80ppm per round trip (see Fig. 4.5). This depends on polishing and coating technologies

-ii) Absorptions on the mirrors coatings ~0.3 ppm, i.e., 3ppm per round trip

-iii) Absorption by the ion beam ~3 ppm

leading to an enhancement factor S= 6300 with a finesse of : F=10000.

According to Eq. 2, the cavity can reach 3 MW of intra-cavity power with an input power of 500W.

In any case, interference phenomena put severe constraints on both spatial and spectral properties of the laser. In fact, the laser used needs a well-defined Gaussian mode, i.e. single mode, and a well-defined frequency, i.e. single frequency.

None of the existing laser sources can guarantee such a high power for a single mode and single frequency beam. The appropriate solution would be to use a low power laser which is amplified in a high power optical fiber.

It has already been shown that fiber master oscillator power amplifier (MOPA) is a promising technology able to provide 100W of input laser power without adding any overwhelming phase or amplitude noise.

Coating absorption and mirror thermal study

For each mirror, about 1 W of the 3 MW intra-cavity power is absorbed by the mirrors coatings, which gives rise to important temperature gradient and consequently thermo-elastic distortions (see figure 4.6). This is expected to distort mirrors surfaces in a non-spherical way, to change their optical behavior: their curvature is modified and, more importantly, their scattering losses are increased, reducing the cavity enhancement factor.

Figure 4.6: Thermo-elastic deformation of the mirror by 3MW of intra-cavity photon power.

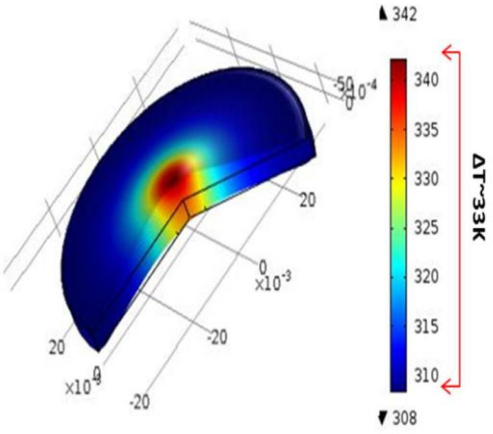

Thermal Compensation Systems (TCS) are therefore required to recover the initial zero-power cavity conditions. Different solutions are proposed:

- Cool down the back side of the mirror. This solution can only be applied to totally reflective mirrors and as such is not effective for the input mirror.

- Compensate the distortion by applying a mechanical stress.

- Compensate the mirror distortion by heating the back face of the mirror in order to achieve a compensating distortion

The thermal analysis conducted below considers a mirror radius of a=4cm and width *h*=5mm which reduces the expansion effect; it is illuminated with a photon beam of radius *w*=1cm with an absorption rate of 0.3 ppm. The cavity length (round trip) being 100 m, we choose the stable configuration in which all the mirrors are flat excepted the end cavity mirror which has a 1 km curvature radius.

The first step is to calculate the steady state temperature distribution within the mirror using COMSOL software. The second step is to compute the thermo-elastic displacement field. We concentrate on the z component (the direction of the light propagation) of the displacement field u_z (r,θ) on the intra-cavity mirror surface, where (r,θ) are the polar coordinates of the mirror surface.

The mirror is considered as a fused silica cylinder maintained on its edge. It receives a heat flux on its intra-cavity side corresponding to the absorption of the laser beam modeled by a Gaussian shape heat flux. At the wavelength corresponding to the temperatures considered here, silica is opaque and can be considered as a black body. The heat exchange with the external environment

is made through radiation between the mirror's surface and the vacuum vessel with a uniform and constant temperature T_0 = 300K.

The obtained displacement field u_z on the intracavity mirror side is then used to determine the residual optical behavior of the mirrors.

Study of Thermal Compensation Systems (TCS):

The TCS proposed here involves heating the central part of the back side of the mirror with a heater at a temperature Tc and diameter b (see Fig. 4.7). The calculation has been performed for different values of the heater diameter b and temperature.

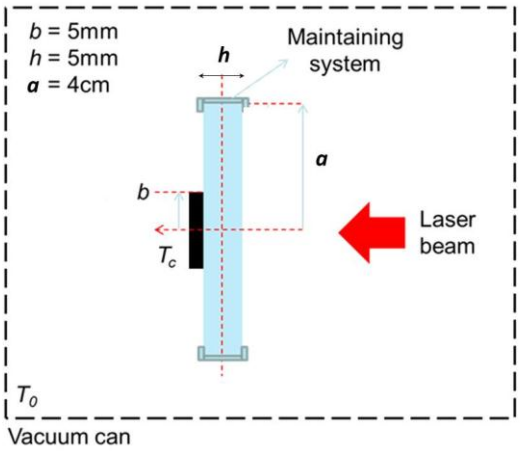

Figure 4.7: Thermal Compensation System with central heater implemented on the back side of the mirror (outside the cavity). The heater radius is 5mm, the mirror thickness is 5mm, and the intra-cavity photon beam power (Laser beam) is 3MW.

Without any correction system, the longitudinal temperature gradient induces a mirror expansion oriented towards the intra-cavity side (see Fig. 4.8 – Without TCS). With a central heater at a temperature Tc = 690 K and h=1cm (see Fig. 4.8 With TCS), the expansion takes place at the back side of the mirror (outside the cavity), while the distortion on the cavity side is nearly paraboloid.

A rough estimation of scattering losses is given by:

$$\Lambda = 4\left(\frac{2\pi}{\lambda}\right)^2 \sigma^2$$ where σ is peak to valley distortion.

The important peak to valley distortion observed without heater (see Fig. 4.9 –Without TCS) is considerably reduced (by a factor 20) leading to a much lower scattering loss (reduction by a factor 400).

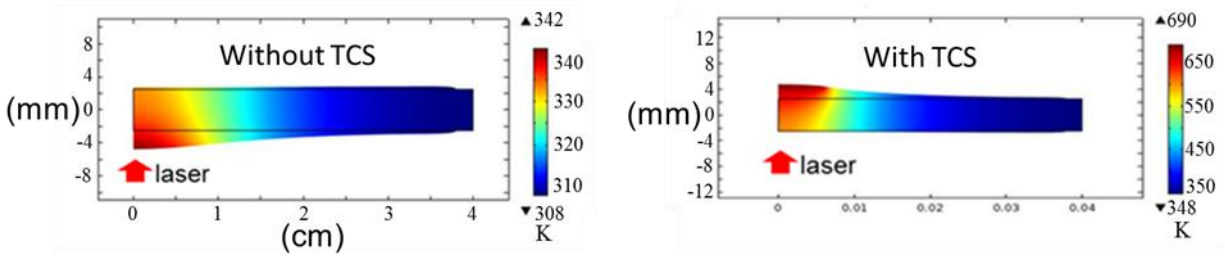

Figure 4.8: Mirror temperature field and distortion with/without compensation system.

With the central heater, the cavity enhancement factor is kept higher than 5000 corresponding to an input Laser power of P_0= 600 W for 3MW of intra-cavity power.

Moreover, at the minimum of the scattering losses (Tc=690 K), the radius of curvature has changed from R = 1 km (initial value) up to L≃ 5.8 km. This central heating is only valid for the totally reflective mirrors since the TCS acts on the outer face of the cavity. Further investigations are to be conducted: (i) for the case of input mirrors for which the central part must be kept clear (see Fig. 4.5); an indirect heating via a CO_2 laser beam could be an interesting alternative. Moreover, we note that the scattering losses estimated above represent an upper losses limit within the cavity. Indeed, the scattered light from one mirror can be re-coupled to the cavity mode when reflected by another mirror.

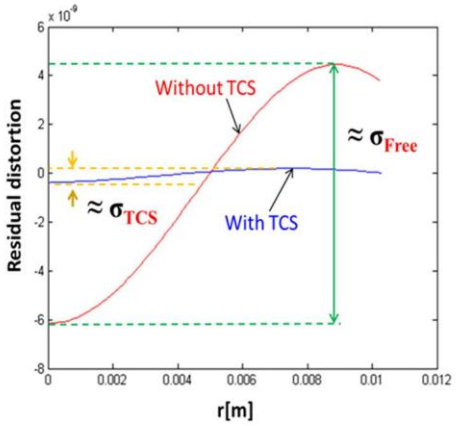

Figure 4.9: Mirror residual distortion corresponding to the thermal distortion from which the spherical term is subtracted. This is responsible of the scattering losses.

5- HIGH VOLTAGE HOLDING IN VACUUM

IRFM, IRSAMC(LCAR), LPGP, SUPELEC laboratories

As one of the goals of SIPHORE is to allow the DEMO neutral beam system to accelerate beams to 2 MeV, via -1 MV, 0 and +1MV potentials, voltage holding in vacuum is an issue. The current design of the ITER bushing that must provide the voltages to the 1 MV accelerator is of considerable size and expense and is also untested. Because the accelerator for SIPHORE aims to accelerate the beams over a single gap, the bushing can be simplified [16] because there is no need to provide five intermediate voltages through a single bushing.

The project HVIV (High Voltage holding In Vacuum) aims to develop and demonstrate a simplified compact bushing (see Fig.5.1) in order to hold the 1 MV; an estimated 5 insulators are required that are separated by metal flanges. A total of 10 insulators are used because the bushing is a closed gas-tight system and 1 MV insulation must be provided between the SF_6 and the vacuum side of the beamline vessel. The gas-tight bushing allows its interior to be filled with low-pressure gas (~0.01 to 0.05 Pa) that serves to suppress dark current [74,75]. This dark current is an electron current, it results from an electron field emission process [74] which occurs on the cathode metal surfaces in a vacuum system.

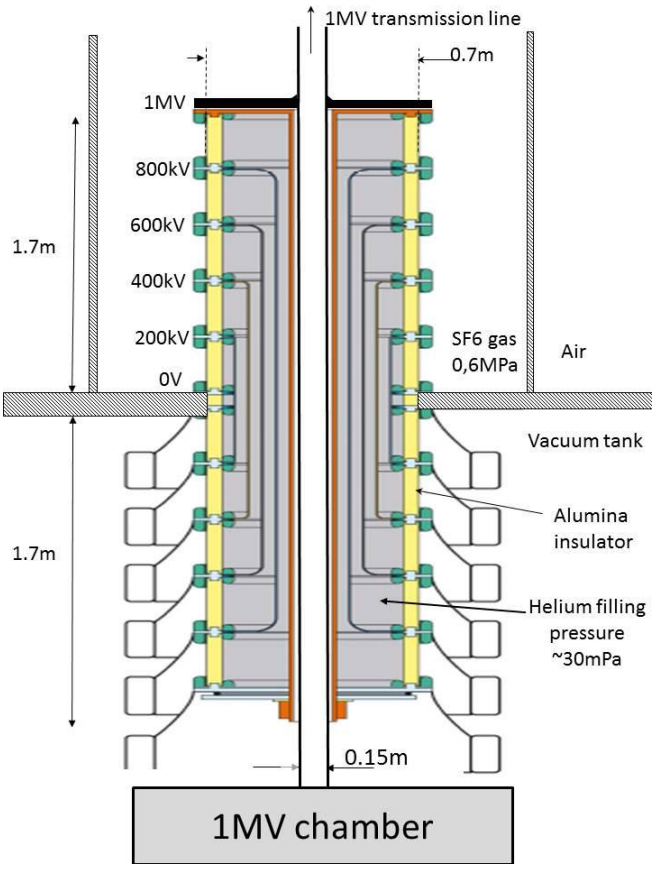

Figure 5.1: 1MV compact Bushing concept

HVIV is a cooperation between 4 French laboratories. At LCAR quantum mechanical calculations are being performed on the electron emission under electric field and the influence of adsorbed gases on the work function, which has a strong influence on the electron emission. At LPGP, theoretical calculations and modelling are being done to highlight the role of surface irregularities, the presence of gas and the influence of nano particles on the electron emission. At SUPELEC small-scale experiments are being performed on the dark current and the influence of gas and surface conditions.

In figure 5.2 the effect of different gases on the electron emission (dark current) generated between electrodes [75] is shown.

It can be seen that when gas is added to the vacuum vessel, the emitted current is significantly reduced. With N_2 and Ar efficient dark current suppression (more than 90%) occurs with a time constant of the order of 1 minute.

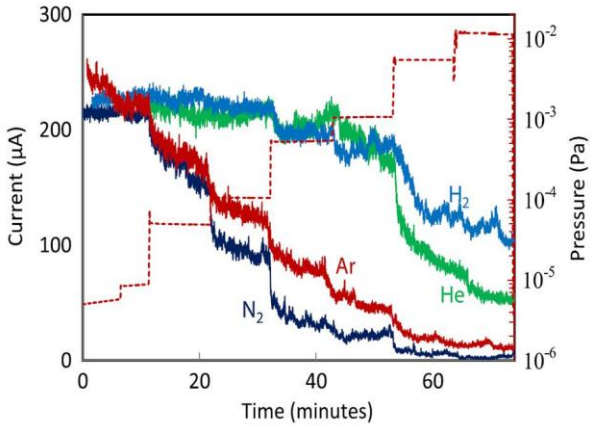

Figure 5.2: Field emission current decrease for four different gases with increasing gas pressure: 2 cm gap distance between electrodes, 30 kV applied voltage.

Finally, IRFM aims at constructing and testing a 400 kV bushing prototype, to be used on their MV test bed. Prior to this, experiments on dark current and voltage holding will be performed on

a single-stage 200 kV bushing under different circumstances, such as the presence of gas to suppress the dark current between electrodes in its inner part (P~30mPa of Helium or Nitrogen), and on prior surface conditioning of the electrodes (heating, glow discharge, cleaning by ultrapure water), in order to sustain the high voltage (ΔV=200kV between electrodes, E~ 50kV/cm) without any breakdown.

HVIV started in 2013. At the origin of the project was the notion that reduction of the dark current with the gas pressure is caused by electric-field induced adsorption of the gas [16]. Soon after the start this idea had to be abandoned. Both from the theoretical side (LCAR) and the experimental side (SUPELEC) it was shown that field induced adsorption of gas cannot be at the origin of the reduction in dark current [75].

While designing and procuring the single stage test bushing, IRFM performed experiments to test the resilience of several electrode materials (Cu, Ti, Mo, stainless steel) against high stored-energy breakdowns. Little difference was found, which means that the cheapest material (stainless steel) is a good choice [76]. Implementation of this bushing on the testbed is now underway and experiments will start soon. Design, procurement and installation of the 2-stage 400 kV bushing are expected to finish in 2016. This bushing should incorporate best practices in terms of surface preparation and gas found during the preceding work. If testing of this bushing is successful, one can consider proceeding with a design for a 1 MV bushing.

ACKNOWLEDGEMENTS

This work benefited from financial support by the French National Research Agency (Agence Nationale de la Recherche; ANR) in the framework of the project ANR-13-BS04-0016-04 (Siphore), ANR-13-BS09-0017-03 (H-Index), ANR- 12-BS09-013 (HVIV), ANR-11-JS09-008 (METRIS) and by the PACA county in the framework of the project "dossier 2011_11042" (PACA Siphore) and "dossier 2012_10357" (PACA-Ging). This work has also been carried out within the framework of the EUROfusion Consortium and has received funding from the European Union's Horizon 2020 research and innovation programme under grant agreement number 633053. The views and opinions expressed herein do not necessarily reflect those of the European Commission. This work was also supported by French Government through a fellowship granted by the French Embassy in Egypt (Institut Français d'Egypte).

REFERENCES

1. M. Q. Tran," The DEMO Heating and Current Drive Programme", to be published in the SOFT 2014 conference proceeding; San Sebastian, Spain
2. T. Franke et al.; "Technological and Physics Assessments on Heating and Current Drive Systems for DEMO", to be published in the SOFT 2014 conference proceeding; San Sebastian, Spain.
3. Romanelli F. et al. Fusion electricity – a roadmap to the realisation of fusion energy; ISBN 978-3-00-0407 20-8 1.
4. R. McAdams; "Beyond ITER: Neutral beams for a demonstration fusion reactor (DEMO); Review of Scientific Instruments 85, 02B319 (2014).
5. G. Giruzzi at al.; "Scenario modelling"; Final Report for TA WP13-SYS01-B, EFDA-Power Plant Physics & Technology
6. RS. Hemsworth et al.;"Status of the ITER neutral beam injection system"; Review of scientific instrument; vol 79, issue 2, pp02C109 - 02C109-5, 2008
7. J. Pamela et al.; "Efficiency and availability driven R&D issues for DEMO"; Fusion Eng. And design 84,2009, pp 194-204
8. G. Fubiani, H.P.L. de Esch, A. Simonin, R.S. Hemsworth ; " Modeling of secondary emission processes in the negative ion based electrostatic accelerator of the

International Thermonuclear Experimental Reactor"; Physical Review Special Topics – Accelerators and beams- 11, 014202 (2008)

9. M. Vandevraye, Ph. Babilotte, C. Drag & C. Blondel; "Laser measurement of the photodetachment cross section of H− at the wavelength 1064 nm"; Phys. Rev. A 90 (2014) 013411.
10. C. Drag, M. Vandevraye, Ph. Babilotte & C. Blondel; "Laser measurement of the photodetachment cross-section of H^- at the wavelength 1064 nm";4th International Symposium on Negative Ions, Beams and Sources, Garching, Germany, 6-10 October 2014, AIP Conference Proceedings, to be published.
11. W. Chaibi, C. Blondel, L. Cabaret, C. Delsart, C. Drag and A.Simonin; "Photo-neutralization of negative ion beam for future fusion reactor"; Negative Ions Beams and Sources, NIBS conference proceeding; Aix en Provence, France, September 2008.
12. D.Fiorucci, W.Chaibi, C.N.Man , and A.Simonin; "Optical Cavity Design for application in NBI systems of the future generation of Nuclear Fusion reactors"; 4th International Symposium on Negative Ions, Beams and Sources, Garching, Germany, 6-10 October 2014, AIP Conference Proceedings, to be published
13. G. Cartry, K Achkasov, C. Pardanaud, A. Gicquel, A. Simonin, J.M. Layet; "H^-/D^- negative-ion surface production on diamond materials in low-pressure Cs-free H_2/D_2 plasmas"; 4th International Symposium on Negative Ions, Beams and Sources, Garching, Germany, 6-10 October 2014, AIP Conference Proceedings, to be published
14. K. Achkasov, R. Bisson, G. Cartry, A. Gicquel, JM. Layet, O. Saidi, A. Simonin; " Thermodesorption analysis: input in understanding of negative ion surface production"; 4th International Symposium on Negative Ions, Beams and Sources, Garching, Germany, 6-10 October 2014, AIP Conference Proceedings, to be published
15. H.P.L. de Esch, A. Simonin, C. Grand; "High Stored-Energy Breakdown Tests on Electrodes made of Stainless Steel, Copper, Titanium and Molybdenum"; 4th International Symposium on Negative Ions, Beams and Sources, Garching, Germany, 6-10 October 2014, AIP Conference Proceedings, to be published
16. A.Simonin, H. de Esch, L. Doceul, L. Christin, F. Faisse, F. Villecroze ; "Conceptual design of a high-voltage compact bushing for application to future N-NBI systems of fusion reactors"; Fusion Engineering and Design 88 (2013)
17. G. Giruzzi, J.F. Artaud, M. Baruzzo, T. Bolzonella, E. Fable, L. Garzotti, I. Ivanova-Stanik, R. Kemp, D.B. King, M. Schneider, R. Stankiewicz, W. Stępniewski, P. Vincenzi, D. Ward, R. Zagórski; "Modelling of pulsed and steady-state DEMO scenarios"; paper submitted to Nuclear Fusion, 2015.
18. U. Fantz et al.; « Physical performance analysis and progress of the development of the negative ion RF source for the ITER NBI system"; Nucl. Fus. 49, 2009, 125007, 9pp
19. A. Simonin, L. Christin, H.P.L. De-Esch, R. Futtersack, P. Garibaldi and F. Villecroze; "Mirror-like plasma confinement for a uniform large negative ion source"; Nucl. Fusion 52 (2012) 063003 (7pp)
20. G. Hagelaar, G.Fubiani, and J.P. Boeuf, Model of an inductively coupled negative ion source – I General model description, Plasma Sources Sci. Technol. 20, 015001 (2011)

21. J P Boeuf, G J M Hagelaar, P Sarrailh, G Fubiani and N Kohen, “Model of an inductively coupled negative ion source – II Application to an ITER-type source”, Plasma Sources Sci. Technol. 20, 015002 (2011)
22. G. J. M. Hagelaar and N. Oudini, “Plasma transport across magnetic field lines in low-temperature plasma sources”, 2011 Plasma Phys. Control. Fusion 53 124032
23. St Kolev, G J M Hagelaar, G Fubiani and J-P Boeuf ; “Physics of a magnetic barrier in low-temperature bounded plasmas”; Plasma Sources Sci. Technol. 21 025002 (2012)
24. G Fubiani, G J M Hagelaar, St Kolev and J-P Boeuf; “Modeling a high power fusion plasma reactor-type ion source: Applicability of particle methods”, Phys. Plasmas 19 043506
25. A.Simonin, P. Garibaldi; “Cybele : A large size ion source of modular construction for the Tore-Supra diagnostic injector;”; RSI 77 (March 2006), number 03A525
26. F. Chen; “ Langmuir probe measurements in the intense RF field of a helicon discharge”; Plasma Sources Sci. Technol. 21 (2012) 055013
27. D Bohm; “ The Characteristics of Electrical Discharges in Magnetic Field”; ed. A Guthrie and R Wakerling; 1949 (New York: McGraw-Hill)
28. JP. Boeuf, B. Chaudhury;”Rotating instability in low temperature Magnetized plasmas”;PRL111,155005 (2013)
29. J. P. Boeuf, B. Chaudhury, and L. Garrigues, Physics of a magnetic filter for negative ion sources. I. Collisional transport across the filter in an ideal, 1D filter, Physics of Plasmas 19, 113509 (2012).
30. J. P. Boeuf, J. Claustre, B. Chaudhury, and G. Fubiani, Physics of a magnetic filter for negative ion sources. II. E × B drift through the filter in a real geometry, Physics of Plasmas 19, 113510 (2012).
31. J.P. Boeuf, B Chaudhury; Phys. Rev. Lett. 111, 155005 (2013)
32. G. Hagelaar, R. Futtersack, R. Baude, "Fluid model of magnetic drifts and instabilities in magnetized low-temperature plasma sources", 67th Gaseous Electronic Conference, 3-7 November 2014, Raleigh, CN, USA.
33. Ph-D thesis Romain Futtersack, “Modélisation fluide du transport magnétisé dans les plasmas froids” ; 2014 ; Laplace Laboratory ; Paul Sabatier University ; Toulouse ; France.
34. R. W. Boswell, Plasma Phys. Controlled Fusion 26, 1147 (1984).
35. U. Fantz and W. Bohm, RF workshop at 14th ICIS (2011).
36. D. G. Miljak and F. F. Chen, Plasma Sources Sci. Technol. 7, 61 (1998).
37. T. Watari et al., Phys. Fluids 21, 2076 (1978).
38. R. W. Boswell, Phys. Lett. 33A, 457 (1970).]
39. D. G. Miljak and F. F. Chen, Plasma Sources Sci. Technol. 7, 61 (1998)
40. Ph. Guittienne et al., Journal of Applied Physics 98, 083304 (2005).
41. Ch. Hollenstein et al., Plasma Sources Sci. Technol. 22, 055021 (2013).
42. Ph. Guittienne et al., Phys. Rev. Lett. 111, 125005 (2013).
43. Fantz U, Franzen P and Wünderlich D 2012 Development of negative hydrogen ion sources for fusion: Experiments and modelling Chem. Phys. 398 7–16
44. Franzen P, Gutser R, Fantz U, Kraus W, Falter H, Fröschle M, Heinemann B, McNeely P, Nocentini R, Riedl R, Stäbler A and Wünderlich D 2011 Performance of

multi-aperture grid extraction systems for an ITER-relevant RF-driven negative hydrogen ion source Nucl. Fusion 51 073035
45. Schiesko L, McNeely P, Fantz U, Franzen P and NNBI Team 2011 Caesium influence on plasma parameters and source performance during conditioning of the prototype ITER neutral beam injector negative ion source Plasma Phys. Control. Fusion 53 085029
46. Fantz U, Gutser R and Wimmer C 2010 Fundamental experiments on evaporation of cesium in ion sources Rev. Sci. Instrum. 81 02B102
47. Bacal M 2006 Physics aspects of negative ion sources Nucl. Fusion 46 S250–9
48. Dudnikov V SU patent application C1.H013/04
49. Dudnikov V 2012 Forty years of surface plasma source development Rev. Sci. Instrum. 83 02A708
50. Roncin P, Borisov A, Khemliche H, Momeni A, Mertens A and Winter H 2002 Evidence for F^- Formation by Simultaneous Double-Electron Capture during Scattering of F+ from a LiF(001) Surface Phys. Rev. Lett. 89
51. Winter H, Mertens A, Lederer S, Auth C, Aumayr F and Winter H 2003 Electronic processes during impact of fast hydrogen atoms on a LiF() surface Nucl. Instrum. Methods Phys. Res. Sect. B Beam Interact. Mater. At. 212 45–50
52. Schiesko L, Carrère M, Cartry G and Layet J-M 2008 Experimental study and modeling of the electron-attracting sheath: The influence of secondary electron emission Phys. Plasmas 15 073507
53. Schiesko L, Carrère M, Layet J-M and Cartry G 2009 Negative ion surface production through sputtering in hydrogen plasma Appl. Phys. Lett. 95 191502
54. Schiesko L, Carrère M, Layet J-M and Cartry G 2010 A comparative study of H − and D − production on graphite surfaces in H_2 and D_2 plasmas Plasma Sources Sci. Technol. 19 045016
55. Kumar P, Ahmad A, Pardanaud C, Carrère M, Layet J M, Cartry G, Silva F, Gicquel A and Engeln R 2011 Enhanced negative ion yields on diamond surfaces at elevated temperatures J. Phys. Appl. Phys. 44 372002
56. Cartry G, Schiesko L, Hopf C, Ahmad A, Carrère M, Layet J M, Kumar P and Engeln R 2012 Production of negative ions on graphite surface in H_2/D_2 plasmas: Experiments and srim calculations Phys. Plasmas 19 063503
57. Ahmad A, Dubois J, Pasquet T, Carrère M, Layet J M, Faure J B, Cartry G, Kumar P, Minéa T, Mochalskyy S and Simonin A 2013 Negative-ion surface production in hydrogen plasmas: modeling of negative-ion energy distribution functions and comparison with experiments Plasma Sources Sci. Technol. 22 025006
58. Ahmad A, Pardanaud C, Carrère M, Layet J-M, Gicquel A, Kumar P, Eon D, Jaoul C, Engeln R and Cartry G 2014 Negative-ion production on carbon materials in hydrogen plasma: influence of the carbon hybridization state and the hydrogen content on H − yield J. Phys. Appl. Phys. 47 085201
59. Wurz P, Schletti R and Aellig M R 1997 Hydrogen and oxygen negative ion production by surface ionization using diamond surfaces Surf. Sci. 373 56–66
60. Fuselier S A, Bochsler P, Chornay D, Clark G, Crew G B, Dunn G, Ellis S, Friedmann T, Funsten H O, Ghielmetti A G, Googins J, Granoff M S, Hamilton J W, Hanley J,

Heirtzler D, Hertzberg E, Isaac D, King B, Knauss U, Kucharek H, Kudirka F, Livi S, Lobell J, Longworth S, Mashburn K, McComas D J, Möbius E, Moore A S, Moore T E, Nemanich R J, Nolin J, O'Neal M, Piazza D, Peterson L, Pope S E, Rosmarynowski P, Saul L A, Scherrer J R, Scheer J A, Schlemm C, Schwadron N A, Tillier C, Turco S, Tyler J, Vosbury M, Wieser M, Wurz P and Zaffke S 2009 The IBEX-Lo Sensor Space Sci. Rev. 146 117–47

61. Scheer J A, Wieser M, Wurz P, Bochsler P, Hertzberg E, Fuselier S A, Koeck F A, Nemanich R J and Schleberger M 2006 Conversion surfaces for neutral particle imaging detectors Adv. Space Res. 38 664–71
62. Lienemann J, Blauth D, Wethekam S, Busch M, Winter H, Wurz P, Fuselier S A and Hertzberg E 2011 Negative ion formation during scattering of fast ions from diamond-like carbon surfaces Nucl. Instrum. Methods Phys. Res. Sect. B Beam Interact. Mater. At. 269 915–8
63. Vector Fields OPERA-3D software, Cobham plc, Brook Road, Wimborne, Dorset, BH21 2BJ, UK. http://operafea.com/
64. G. Fubiani, H. P. L. de Esch, R. S. Hemsworth, A. Simonin.; Physical Review special topics; Accelerators and beams 11, 014202 (2008)
65. A. Lifschitz, A. Revel, L. Caillault, and T. Minea, Numerical study of beam propagation and plasma properties in the ITER Neutral Beam Injector, Nucl. Fusion 54 (2014) 043020,
66. A. Revel, S. Mochalskyy, L. Caillault, A. Lifschitz, and T. Minea, Comparison between realistic and ideal negative ion beamlets in the ITER-like accelerator of NBI, Nuclear Fusion 53 (2013) 073027
67. S. Mochalskyy, A. Lifschitz, and T. Minea, 3D modelling of negative ion extraction from a negative ion source, Nuclear Fusion 50 (2010) 105011
68. S. Mochalskyy, A. Lifschitz, and T. Minea, Extracted current saturation in negative ion sources J. Appl. Phys. 111 (2012) 113303
69. S. Mochalskyy, D. Wünderlich, B. Ruf, P. Franzen, U. Fantz, and T. Minea, 3D numerical simulations of negative hydrogen ion extraction using realistic plasma parameters, geometry of the extraction aperture and full 3D magnetic field map, Rev. Sci. Instrum. 85 (2014) 02B301
70. S. Mochalskyy, D. Wuenderlich, U. Fantz, P. Franzen, T. Minea, Towards a realistic 3D simulation of the extraction region in ITER NBI relevant ion source, Nucl. Fusion 56 (2014) 105001
71. H.-P. Popp & S. Kruse, J. Quant. Spectrosc. Radiat. Transfer 16 (1976) 683
72. C. C. Havener, M. S. Huq, H. F. Krause, P. A. Schulz, & R. A. Phaneuf, Phys. Rev. A 39 (1989) 1725
73. Kent M. Ervin et al., J. Chem. Phys. 91 (1989) 5974 ; J. B. Kim, et al., J. Phys. Chem. A 103 (1999) 10833
74. P. Massmann, D. Boilson, H. De Esch, R. Hemsworth, L. Svensson, Voltage Holding and Dark Currents in the Cadarache 1MV Ion Beam Facility, 20th International Symposium on Discharges and Electrical Insulation in Vacuum - Tours (France), 30/06/02 - 5/07/02

75. K. Almaksour, M. J. Kirkpatrick, Ph. Dessante, E. Odic, A. Simonin, H. P. L. de Esch, B. Lepetit, D. Alamarguy, F. Bayle, Ph. Teste, Experimental study of the reduction of field emission by gas injection in vacuum for accelerator applications, Physical Rev. Sp. Topics - Accelerators and Beams 17, 103502 (2014)
76. H.P.L. de Esch, A. Simonin and C. Grand, High Stored-Energy Breakdown Tests on Electrodes made of Stainless Steel, Copper, Titanium and Molybdenum, 4th International Symposium on Negative Ions, Beams and Sources, Garching, Germany, 6-10 October 2014, AIP Conference Proceedings, to be published
77. Cs-doped Mo molybdenum as surface converter for H^- / D^- generation in NNBI sources: from long term stability to the surface generation mechanisms
78. L. Schiesko, G. Cartry, C. Hopf, T. Höschen, G. Meisl, W. Jacob, O. Encke, T. Dürbeck, P. Franzen, B. Heinemann, P. Amsalem , K. Achkasov and U. Fantz; "Cs-doped Mo molybdenum as surface converter for H- / D- generation in NNBI sources: from long term stability to the surface generation mechanisms"; 4th International Symposium on Negative Ions, Beams and Sources, Garching, Germany, 6-10 October 2014, AIP Conference Proceedings, to be published